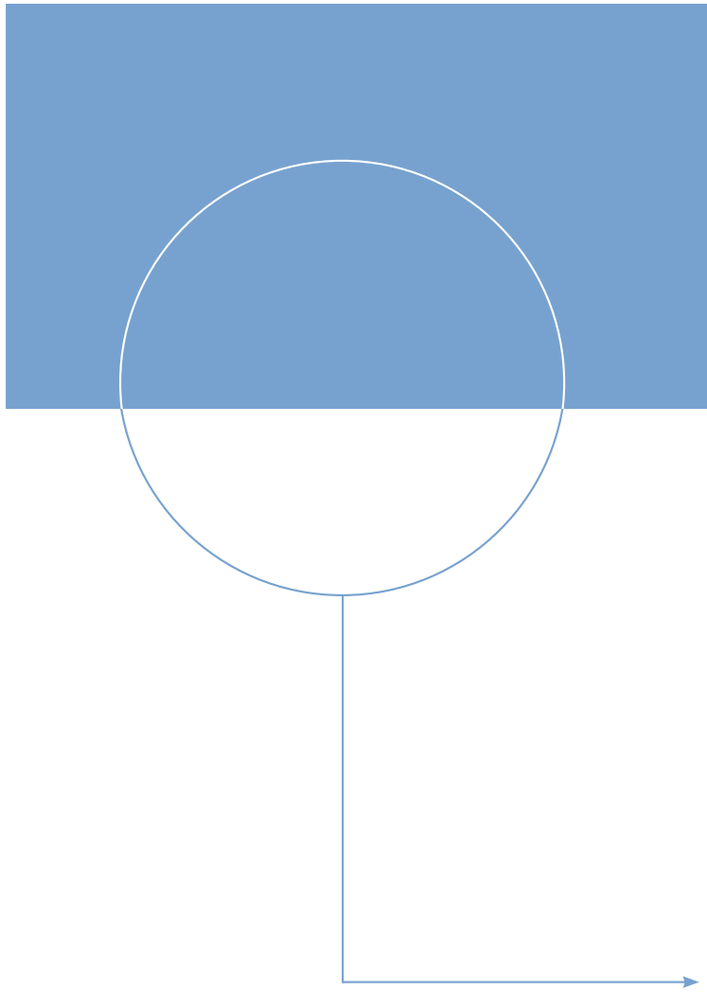

Master's thesis

2019

Anita Otto Ringia

NTNU
Norwegian University of
Science and Technology
Faculty of Engineering
Department of Geoscience and Petroleum

Anita Otto Ringia

Numerical Study Using Computational Fluid Dynamics of the Cooling Process inside a Subsea Oil Storage Tank to Evaluate Wax Appearance Vulnerability

August 2019

NTNU
Norwegian University of
Science and Technology

NTNU
Norwegian University of
Science and Technology

NTNU

Norwegian University of
Science and Technology

Numerical Study Using Computational Fluid Dynamics of the Cooling Process inside a Subsea Oil Storage Tank to Evaluate Wax Appearance Vulnerability

Anita Otto Ringia

Petroleum Engineering
Submission date: August 2019
Supervisor: Milan Stanko, IPT
Co-supervisor: Audun Faanes, Equinor Research Center Rotvoll
Knut Sveberg, Equinor Research Center Rotvoll

Norwegian University of Science and Technology
Department of Geoscience and Petroleum

Abstract

The work described in this thesis is focused on studying temperature distribution within a subsea oil storage tank to locate areas that are vulnerable to wax appearance. The analysis uses Computational Fluid Dynamics (CFD) done in ANSYS Technology Inc's Software FLUENT. The study involves numerical simulations of oil storage during both flow and no-flow conditions at a constant crude oil composition.

A simplified two-axes symmetry geometry is used for the simulations to reduce computational cost. The simulations are performed under laminar unsteady state conditions with a 200 mm mesh size after grid independence testing. Results reveal that cooling starts at the bottom of the bag in both flow and no-flow conditions as heat is lost to the surrounding seawater. Wax appearance is considered not favorable in the bulk fluid during flow since the bulk temperature is above the Wax Appearance Temperature (WAT). However the temperature of side and bottom boundaries of the bag for flow and all walls for no-flow reach the WAT. This makes the walls vulnerable to wax deposition.

Sensitivity analysis is conducted to explore how much variations in the flow rate impact the results. The analysis involves mass inlet flow rates of 11.01 kg/s, 22.02 kg/s and 33.03 kg/s. Low rates are seen to slow down molecular motion of the warmer molecules thus favoring the cooling process. Upper wall boundaries are observed not to reach WAT for the higher rates. Only with 11.01 kg/s, WAT is been reached at the upper boundaries.

The results obtained in this report may be subject to uncertainties due to lack of experimental data to validate the numerical findings. However, these results may still guide in devising of the optimum operating strategies to mitigate wax deposition in the tank. Even though the origin of this report is to locate areas vulnerable to wax appearance at a constant crude oil composition and a stationary bottom boundary, it remains for future work to actually implement wax deposition models to determine wax thickness. Also multiphase models may be implemented considering that oil usually flows with water and sometimes gas. Moreover, a moving boundary at the bottom of the bag may be taken into consideration to study the effect on the fluid dynamics.

Preface

This Masters thesis is written in partial fulfillment for the award of a Masters degree in Petroleum Engineering at the Department of Geoscience and Petroleum, Norwegian University of Science and Technology, Trondheim. It is a continuation of the work that started in the Specialization Project (TPG4560).

First I would like to appreciate Equinor Research Centre in Rotvoll, Trondheim for giving me an opportunity to work on this exciting concept and also providing experience support with the ansys FLUENT software used in this thesis work.

I would also like to deeply appreciate my supervisor from the Norwegian University of Science and Technology, Milan Stanko for the tireless guidance and qualitative feedback throughout my project and this Masters thesis. Your contributions towards the success of this work are invaluable and I greatly acknowledged them.

Many thanks to my co-supervisors from Equinor-Trondheim Norway, Audun Faanes and Knut Sveberg that have initiated the terms and goals of this work, I do appreciate your insightful suggestions on how to get the work done. I also thank Torstein Austvik who continually provided help to my questions during this thesis work.

Last but not least, with a grateful heart, I would like to remember Equinor and NORAD for the financial support under ANTHEI project. This funding has helped me become financially stable throughout my studying period and thus was able to concentrate on my studies well.

I hereby certify that this work is exclusively my own.

Anita Otto Ringia

Dedication

I dedicate this work to my lovely parents Otto Ludovick Ringia and Asteria Stephen Ringia for all their sacrifices, efforts and an endless support given to me throughout this thesis. Without their prayers, I could not have achieved so much. May the Almighty God grant them many more joyful years and abundant blessings.

Contents

List of Tables vii

List of Figures ix

Nomenclature x

Abbreviations xii

1 Introduction 1

1.1 Background . . . 1
1.2 Problem Statement . . . 3
1.3 Objectives . . . 4
1.3.1 Main Objective . . . 4
1.3.2 Specific Objectives . . . 4

2 Wax 5

2.1 Wax Appearance . . . 5
2.2 Wax Deposition . . . 6
2.3 Wax Deposition Mechanisms . . . 7
2.3.1 Molecular Diffusion . . . 7
2.3.2 Shear Dispersion . . . 7
2.3.3 Gravity Settling . . . 7
2.3.4 Brownian Motion . . . 8

3 Subsea Storage Tank 9

3.1 Principle of Operation . . . 11

4 Convection Heat Transfer 12

5 Computational Fluid Dynamics (CFD) 15

5.1 CFD Simulations Solving Procedures . . . 16
5.1.1 Pre-processor . . . 16
5.1.2 Processor . . . 17
5.1.3 Post-processor . . . 18

6 Numerical Simulations 19

6.1 Geometry Generation . . . 19
6.2 Mesh Generation . . . 23
6.3 Setting Simulations . . . 24
6.4 Solving . . . 26

7 Post Processing **27**

8 Grid Independence Study **29**

9 Results and Discussion **30**
9.1 Grid Independence Study 30
9.2 No-flow Simulations 33
9.2.1 Steady State Solution 37
9.3 Flow Simulations 39
9.4 Effect of Flow 43
9.5 Sensitivity Analysis 45
9.6 Shortcomings 49
9.6.1 Shortcomings in the Implemented Models 49
9.6.2 Shortcomings in the Conducted Work 49

10 Summary **50**

11 Future Work **52**

References **53**

Appendix **55**

A Convenctive Heat Transfer Coefficient **55**
A.1 Horizontal Plate 55
A.2 Vertical Cylinder 56
A.3 Sphere 58

B Convective Heat Transfer Coefficient Calculations **59**

C Step-by-step FLUENT **60**

D Fluid Properties Used in FLUENT **61**

E Temperature Profiles **63**
E.1 Simulations with 11.01 kg/s 64
E.2 Simulations with 22.02 kg/s 65
E.3 Simulations with 33.03 kg/s 66

F Velocity Profiles **67**
F.1 No-Flow Simulations 68
F.2 Simulations with 11.01 kg/s 69

F.3 Simulations with 22.02 kg/s 70
F.4 Simulations with 33.03 kg/s 71

G Enlarged Figures of the Velocity Profiles for the Comparison Study between No-Flow and Flow Steady State Solutions 72

H Steady State Solution of No-Flow Simulations 74

List of Tables

1 Physical Models 24
2 Inputs for Piecewise-Polynomial Functions [15] 25
3 Properties of Protective Structure and Bag [15] 25
4 No-Flow Cases Run by Refining Grid Size 26
5 Flow Cases Run by Altering Flow 26
6 Summary of Fluid Temperature at Point X Showing Improved Accuracy as a Result of Refining Mesh 31

List of Figures

2.1 Pressure-Temperature wax precipitation envelope [8] 6
3.1 Subsea storage tank [15] 9
3.2 Dimensions of the subsea storage tank (1:1 scale) [15] 10
3.3 Filling sequence of the bag illustrating the downward movement of the bag and outward displacement of the sea water as oil fills the bag [15]. 11
6.1 Half-full subsea storage tank [15] 19
6.2 3-D subsea storage tank geometry (side view) 20
6.3 One-sixteenth of the full geometry indicating oil (yellow) in the pipe and bag (side view) 21
6.4 A fluid domain used for no-flow simulations in Fluent 22
6.5 Initial Mesh of Fluid domain with 300 mm mesh size (symmetrical plane) . 23
7.1 Symmetrical plane of the geometry showing the positions of Line 1 and Point X 28
9.1 Fluid temperature variations at Point X using 300 mm, 200 mm and 100 mm mesh sizes for coarse, medium and fine mesh elements respectively 30
9.2 Mesh with 200 mm grid size used for the CFD simulations (symmetrical plane) 32
9.3 Average wall temperature profile showing cooling against flow-time for no-flow simulations 33
9.4 Point surface temperature against time for (a) bottom, (b) side and (c) upper boundaries as temperature reaches WAT for no-flow simulations 34
9.5 Bulk fluid temperature evolution at different flow-times during no-flow simulations (a) 100s (b) 471100s (c) 2271100s (d) 4071100s 36
9.6 Bulk fluid temperature at the steady state solution 37
9.7 Bulk fluid temperature variations across line 1 when steady state is reached near the bottom of the bag in no-flow solution 38
9.8 Average wall temperature profile showing cooling against flow-time for flow simulations 39
9.9 Bulk fluid temperature evolution at different flow-times during no-flow simulations (a) 100s (b) 471100s (c) 2271100s (d) 4071100s 40
9.10 Velocity contours at the beginning (a) and steady state (b) for flow simulations 41
9.11 Velocity vectors at the beginning (a) and steady state (b) for flow simulations 42
9.12 Velocity vectors at the steady state of flow simulations (4071100 s) for no-flow (a) and flow (b) solutions 43
9.13 Temperature profiles at the steady state of flow simulations (4071100 s) for no-flow (a) and flow (b) solutions 44
9.14 Bulk fluid temperature variations across line 1 when steady state is reached in flow solutions 45

9.15 Temperature profiles at the beginning (a) and at the steady state of (b) 11.01 kg/s (c) 22.02 kg/s (d) 33.03 kg/s 46
9.16 Velocity vectors at the steady state of flow simulations (4071100 s) for different flow rates. (a) 11.01 kg/s (b) 22.02 kg/s (c) 33.03 kg/s 47
9.17 Wall temperature against time as it reaches WAT for (a) bottom, (b) side and (c) upper boundaries at flow rates of 11.01 kg/s, 22.02 kg/s and 33.03 kg/s . 48
A.1 Buoyancy-driven flows on horizontal cold ($T_S < T_\infty$) and hot ($T_S > T_\infty$) plates. [16] 56
A.2 Corrections for h and $\overline{h}$ on vertical isothermal plates to be applicable for vertical isothermal cylinders [27]. 57
B.1 External natural convective heat transfer coefficients for the wall woundaries 59
D.1 Plot of crude oil density used to obtain coefficients for the Piecewise-polynomial function [15] 61
D.2 Plot of crude oil viscosity used to obtain coefficients for the Piecewise-polynomial function [15] 62
E.1 Bulk fluid temperature evolution at different flow-times during 11.01 kg/s simulations (a) 100s (b) 471100s (c) 2271100s (d) steady state 64
E.2 Bulk fluid temperature evolution at different flow-times during 22.02 kg/s simulations (a) 100s (b) 471100s (c) 2271100s (d) steady state 65
E.3 Bulk fluid temperature evolution at different flow-times during 33.03 kg/s simulations (a) 100s (b) 471100s (c) 2271100s (d) steady state 66
F.1 Velocity vector during no-flow at (a) 100s (b) 471100s (c) 2271100s (d) steady state 68
F.2 Velocity vector during 11.01 kg/s flow at (a) 100s (b) 471100s (c) 2271100s (d) steady state 69
F.3 Velocity vector during 22.02 kg/s flow at (a) 100s (b) 471100s (c) 2271100s (d) steady state 70
F.4 Velocity vector during 33.03 kg/s flow at (a) 100s (b) 471100s (c) 2271100s (d) steady state 71
G.1 Velocity vector from no-Flow Steady state Solution 72
G.2 Velocity vector from Flow Steady state Solution 73
H.1 Steady state solution of no-flow Simulations 74

Nomenclature

Symbol	Description; (Unit)
Γ	Diffusion coefficient
Δ T	Temperature difference between the fluid and the solid surface; (^oC)
μ	Fluid viscosity; (N-s/m^2)
ρ	Fluid density; (kg/m^3)
A	Area of the surface that is in contact with the fluid; (m^2)
A_s	Surface area of a plate; (m^2)
C_p	Heat capacity of the fluid; (J/kg-K)
e	Relative error; (%)
Gr	Grashof number
h	Convective heat transfer coefficient; (W/m^2-K)
k	Thermal conductivity of fluid; (W/m-K)
N_u	Nusselt number
P	Perimeter of a plate; (m)
Pr	Prandtl number
p	Pressure; (Pa)
Q	Rate of heat transfer between the fluid and the surface; (W)
Ra	Rayleigh number
Re	Reynolds number

Symbol	Description; (Unit)
S_φ	Source term
T_i	Fluid temperature by given mesh; (K)
T_f	Fluid temperature by fine mesh; (K)
u	Flow velocity of the fluid; (m/s)
u_x	Velocity in x-direction; (m/s)
u_y	Velocity in y-direction; (m/s)
x	Characteristic of the body under consideration-Length, L_c or Diameter, D; (m)

Abbreviations

CAD	Computer Aided Design
CFD	Computational Fluid Dynamics
GRP	Glass-fiber Reinforced Plastics
WAT	Wax Appearance Temperature
WDT	Wax Disappearance Temperature

1 Introduction

1.1 Background

Crude oil is normally stored in tanks, oil tankers or salt mines. Crude oil extracted from offshore fields may be transported onshore through a pipeline or stored in offshore facilities. The former approach tends to become less favorable in remote locations. Pipeline transportation also comes with risks such as oil spills and explosions.

The offshore storage of oil can be temporary or permanent. Traditionally, crude oil is stored in the floating facilities until is offloaded onto a tanker or a pipeline for transportation ashore. This traditional method leads to additional weight and size on the platform resulting in cost increase. Floating storage consumes a lot of fuel and thus increasing CO_2 emissions. In addition, it demands permanent offshore personnel for maintenance of the infrastructure. Due to these limitations, an alternative method of storing oil can be a subsea tank at the seafloor. This alternative method is developed to overcome limitations of the floating storage. Its benefits comes from environmental impact as it requires less fuel consumption compared to the floating storage. It also improves total safety as subsea storage demands no permanent personnel offshore and reduces cost due to less facilities needed on the platform [1].

Equinor is an international energy company which is considering to implement the subsea storage of crude oil. The technology is not a flawless solution even though it complies with the company's strategies of *Always safe, High value and Low carbon* [2]. Subsea storage faces flow assurance challenges such as hydrate formation, asphaltenes and wax deposition. These problems can imply restrictions to the storage volume and alternation of the storage properties of the tank. Among these, this study will only focus on wax as it is one of the major flow assurance challenges in the storage of crude oil.

Crude oil extracted from the reservoirs has higher temperature than seawater. During the storage process, cooling of the walls of the subsea tank by surrounding seawater may take place. When the bulk temperature falls below Wax Appearance Temperature (WAT) [3], wax precipitates. Due to temperature gradient, the precipitated wax tend to be deposited on the internal walls. This reduces storage volume and can also change properties of the storage bag as well as increasing pressure drop. Due to these challenges, it is vital to carry out studies that investigate when and where the bulk temperature falls below WAT both during storage and/or filling in and out of the tank.

Wax precipitation is mainly a function of temperature and composition [4]. Thus, this work focuses on the temperature parameter by investigating temperature evolution in the subsea oil storage tank at a constant oil composition. Fluid bulk temperature will be explored both

during flow and no-flow conditions and locations in the tank which become vulnerable to wax precipitation will be suggested. Simulations will be run on ANSYS Technology Inc's software FLUENT. Operating conditions are usually not constant, so sensitivity analysis was carried out to see how different oil flow rates affect temperature distribution in the tank.

1.2 Problem Statement

Wax precipitation in subsea storage tanks occurs when crude oil experience reduced temperature due to the heat lost to the surrounding seawater. When the bulk temperature drops below a certain temperature, usually referred to as the Wax Appearance Temperature (WAT) or the cloud point, wax starts to precipitate out of the oil. This precipitated wax can either remain in the oil, or entrapped in a layer sticking to the internal walls of the tank.

Equinor is considering implementing subsea storage of crude oil. It is vital to take insights into wax precipitation in these tanks as they pose flow assurance challenges when deposited in the tanks. Wax precipitation is mainly a function of oil composition and temperature. The latter is the focus in this thesis. The aim of this thesis is to carry out Computational Fluid Dynamics (CFD) simulations in ANSYS Technology Inc's software called FLUENT to investigate when the temperature in the bulk fluid and the walls reach WAT.

In addition, studies regarding the region in the oil which will be vulnerable to wax precipitation when steady state is reached under both flow and no-flow conditions is conducted. Furthermore, this work takes a look into how flow rate can affect the results. All simulations are run at a constant oil composition and operating conditions of pressure and temperature.

1.3 Objectives

1.3.1 Main Objective

To determine potential wax appearance locations in a subsea oil storage tank using computational fluid dynamics

1.3.2 Specific Objectives

To achieve this, the following are done

i. To perform a grid independence study to obtain a grid size that gives a solution independent of grid density

ii. To compute temperature evolution with time inside the tank and identify locations at which the temperature reaches the wax appearance temperature

iii. To perform simulations considering that there is flow through the tank. Evaluate the effect on the results

iv. To conduct sensitivity analysis to investigate the effect flow rate on the results

2 Wax

Crude oil is a complex mixture that contains heavy components of resins, aromatics, naphthenes, asphaltens and paraffins. Macro-crystalline wax are typically made of long and linear n-paraffin chains. The carbon number distribution of paraffins range typically from $C_{18}H_{38}$ and $C_{70}H_{142}$ [5]. Micro-crystalline waxes contain naphthenes and iso-paraffins. The type of wax present in crude oil is differentiated by its crystal morphology and size [6].

These compounds contained in crude oil are fully dissolved in the mixture at a typical reservoir temperature ranging from 70 - 150 ^{o}C. At these temperatures, crude oil behaves as a Newtonian fluid with a low viscosity. Once the temperature is lowered as crude oil leaves the reservoir, solubility of these wax components in hydrocarbon fluids decreases and starts to form stable wax crystals [7]. These wax particles lead to major flow assurance challenge once deposited on the internal walls of facilities.

2.1 Wax Appearance

Thermodynamic phase behavior of wax is very useful in assessing wax separation from the hydrocarbon containing systems.The key thermodynamic variables that affect wax solubility is composition of the oil and temperature. Pressure changes usually do not have a significant effect on wax precipitation because wax crystals are incompressible and liquid hydrocarbons are slightly compressible [4].

Figure 2.1 shows a typical wax precipitation envelope on a pressure temperature diagram. It is observed that the solid/liquid-phase boundary (wax boundary) is nearly vertical.This illustrates wax precipitation's strong dependence on temperature and weak dependence on pressure. As temperature decreases, solubility of wax decreases. The temperature at which the first precipitation of wax is formed at a given pressure, creating a binary mixture of oil and wax is known as Cloud Point Temperature or Wax Appearance Temperature (WAT) [3].

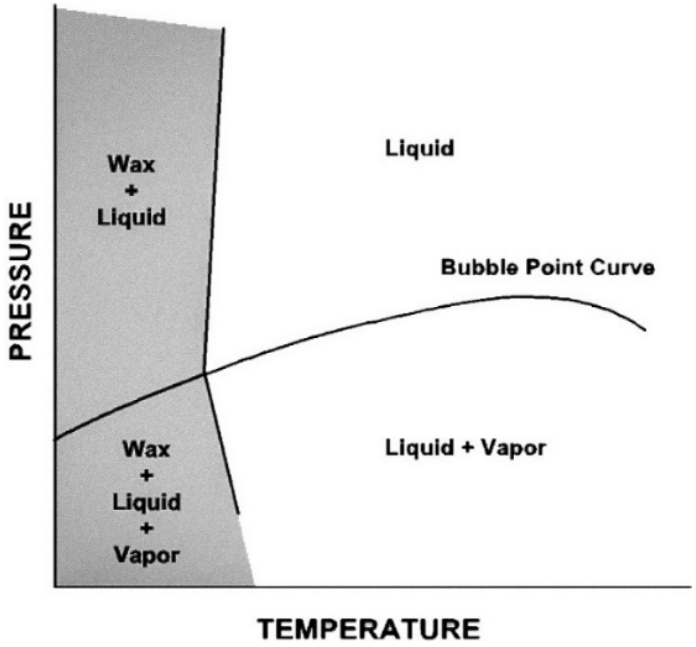

Figure 2.1: Pressure-Temperature wax precipitation envelope [8]

It is also observed that liberation of solution gas from the crude oil as pressure decreases below the bubble-point of oil, increases the cloud-point temperature. This leads to the early wax precipitation and deposition [9].

2.2 Wax Deposition

Wax deposition occurs when a separate solid phase layer is formed below WAT and grow on a cold surface. Under no disturbance as precipitation continues, wax crystals in the crude oil tend to increase in size and quantity and develop an interlocking network of a three-dimensional gel-like structure.

The structure traps a significant amount of oil in the pores which causes a non-Newtonian behaviour and an increase in the effective viscosity of the system. Gel strength and an amount of wax precipitated determine whether oil will flow at a certain temperature [10]. The lowest temperature at which the crude oil forms a stationary gel is referred to as pour point [11].

2.3 Wax Deposition Mechanisms

There are four mechanisms which describe the deposition of wax. These mechanisms are identified as molecular diffusion, Brownian diffusion, shear dispersion, and gravitational settling. Molecular diffusion describes a mechanism from dissolved wax molecules while shear dispersion, gravity settling and Brownian motion from already precipitated wax [12].

2.3.1 Molecular Diffusion

When the wall in contact with crude oil reaches WAT, wax that precipitates out of the solution creates a concentration gradient between the wax remaining in solution in the bulk fluid and amount of dissolved wax at the wall. The concentration gradient then causes the diffused particles to be transported from the bulk fluid to the wall. The diffusing material will be precipitated out of solution at the wall when it reaches the solid/liquid interface[13].

2.3.2 Shear Dispersion

The wax particles move at the mean speed and direction of the oil when are suspended in the flowing oil that is in laminar flow. The shearing of the fluid close to the wall may cause a movement of the wax particles transverse to the direction of local flow due to mutually induced velocity fields. If the particle concentration is high then a significant number of multiparticle collisions will occur and result in net lateral transport and a dispersing of particles [13]. This way the precipitated wax is transported from the turbulent core to the wall.

2.3.3 Gravity Settling

Gravity settling can be a possible mechanism for deposition of wax at the bottom of the tanks or pipes if there is no interaction among the particles. This is because the waxy crystals are denser than surrounding oil phase [13].

2.3.4 Brownian Motion

When small, solid waxy crystals are suspended in oil, there will be a continuous bombardment of the wax solids by thermally agitated oil molecules. Provided there is a concentration gradient of the wax particles, a net transport similar to diffusion will occur due to the Brownian motion [13].

Gravity settling had no significantly effect on the total deposition. Molecular diffusion and shear dispersion are proposed as the predominant mechanisms to describe paraffin deposition.

3 Subsea Storage Tank

Subsea storage tank is a gravity based unit which utilizes a flexible bag for crude oil storage on the sea floor. The bag differentiates the subsea tank from convectional gravity storage units. It introduces a physical barrier between the stored oil and seawater, thus preventing formation of emulsion layer and bacterial growth.

The collapsible bag is further protected by a dome shaped structure. This outer shell accommodates the entire volume of the crude oil to be stored and acts as a second barrier against leakage to the sea. The openings at the base of a protection structure allows free flow of seawater thus designing against water pressure is not required and the unit can as well be deployed at any water depth.

There is a removable hatch located at the top of the protection structure. It is placed to provide sealing and mechanical connection between structure, bag and surrounding environment. The hatch prevents the stored oil from entering the tank's annulus and/or the surrounding environment.The flexible bag can be replaced through the hatch [14].

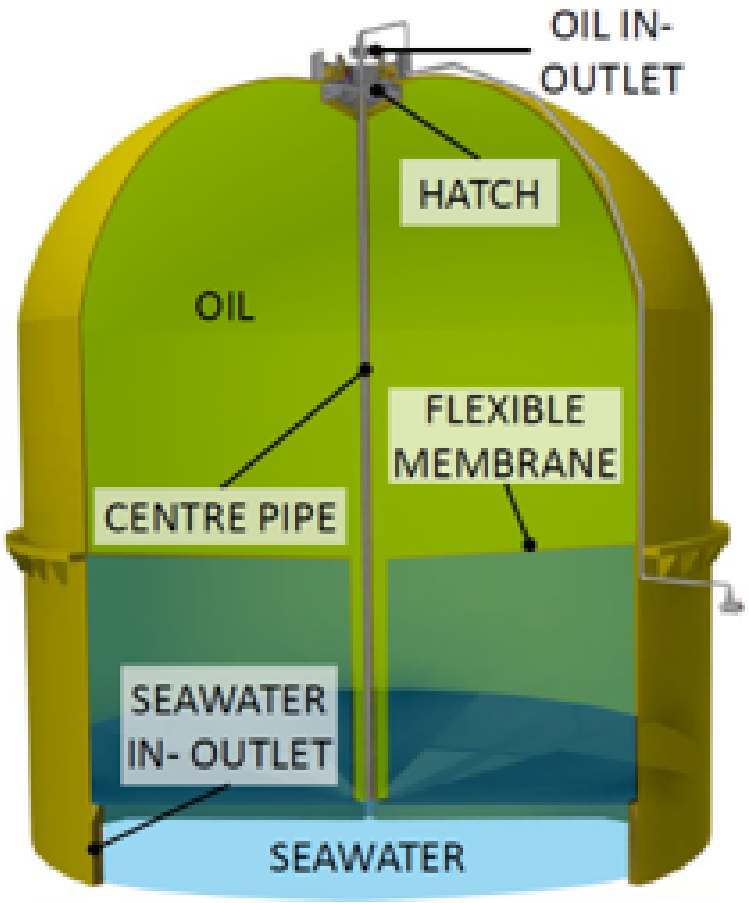

Figure 3.1: Subsea storage tank [15]

The subsea unit to be used by Equinor will have the 50 mm thick protection (dome) structure constructed with GRP material. While the material for the 2 mm flexible bag will be PVC/Nitrile blend and the inner center pipe will be constructed with steel. Figure 3.2 shows the dimensions of the storage unit.

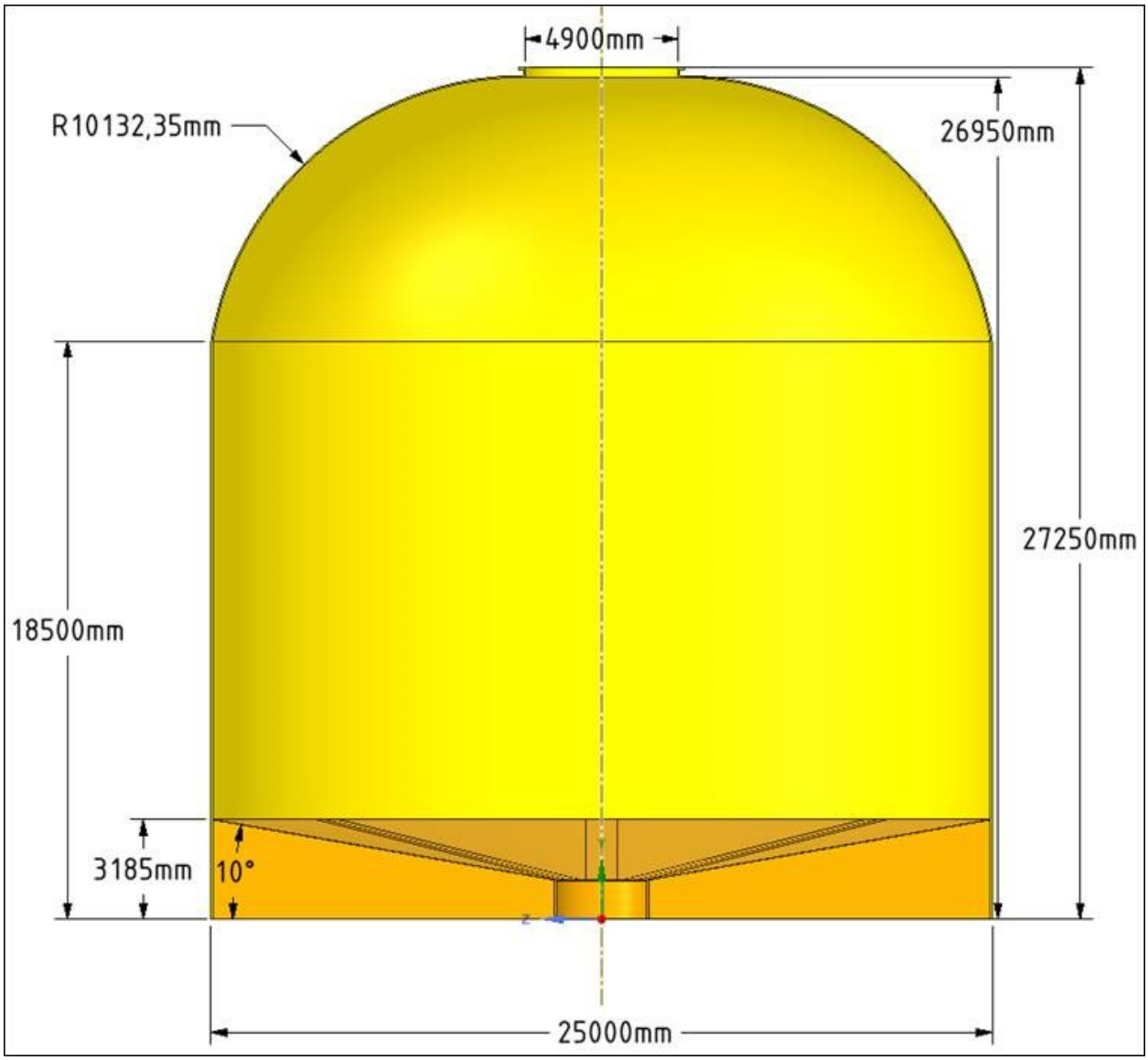

Figure 3.2: Dimensions of the subsea storage tank (1:1 scale) [15]

3.1 Principle of Operation

Before oil is pumped into the collapsible bag, the tank room is filled with seawater. It is the density difference between water and oil causing oil to always fill the bag from the top. The oil in the bag will then displace the water in the dome space resulting in the horizontal downward movement of the bag as illustrated on Figure 3.3.

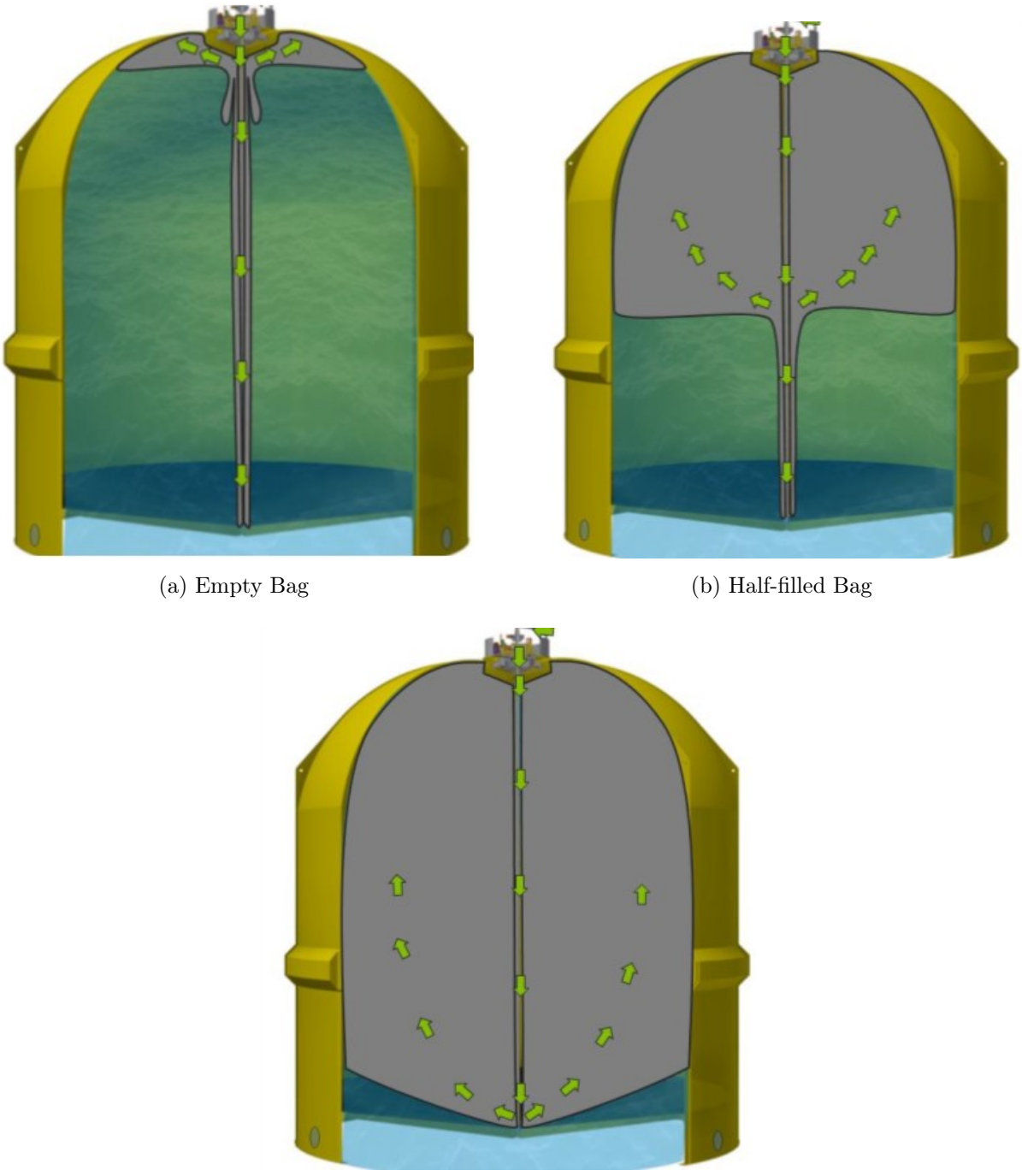

(a) Empty Bag

(b) Half-filled Bag

(c) Full-filled Bag

Figure 3.3: Filling sequence of the bag illustrating the downward movement of the bag and outward displacement of the sea water as oil fills the bag [15].

4 Convection Heat Transfer

Heat transfer takes place either by radiation, conduction or convection. Convective heat transfer been the topic of interest in this study is essentially conducted under fluid motion when there is a temperature difference between the fluid and a solid surface. It occurs when a fluid is in contact with a surface colder or hotter than itself. As the fluid is cooled or heated, its density changes. This difference in density induces a flow due to the force of gravity acting on the density variations and causes the heat transfer to continue.

In the case of an external force like a pump causing fluid flow, it will be called a forced convection. If the fluid motion is caused by natural means such as buoyancy due to density variations within the fluid resulting from temperature distribution then it is natural/free convection. In many real-life applications, both forced and natural convection occur at the same time. This type of convection is known as mixed convection [16].

Newton's Law of Cooling is an equation used for both forced and natural convection heat transfer:

$$\boxed{Q = h.A.\Delta T} \tag{4.1}$$

Where:

- Q - rate of heat transfer between the fluid and the surface; (W)
- h - convective heat transfer coefficient; (W/m^2-K)
- A - area of the surface that is in contact with the fluid; (m^2)
- ΔT - temperature difference between the fluid and the solid surface; (^{o}C)

Determination of the value for the heat transfer coefficient (h) is a significant part of the convective heat transfer calculations. The physical variables on which it depends on can be expressed as: *h=f (fluid properties, velocity field , geometry, temperature etc.)*. This function depends on several parameters, therefore the heat transfer coefficient is usually expressed in terms of correlations involving non-dimensional numbers.

Non-dimensional groupings for forced convection include: Nusselt, Prandtl and Reynolds numbers as expressed in Equations (4.2), (4.3) and (4.4) respectively. For free convection, same parameters apply with an exception of the Reynolds number which is replaced by a parameter called Grashof Number (Equation (4.5a)). This is due to the fact that flow velocity is always zero for the case of natural convection thus the Reynolds number is also zero and is no longer suitable to describe the flow in the system [17].

Nusselt Number: can be viewed as the ratio of the conduction resistance of a material to the convection resistance of the same material.

$$\boxed{Nu = \frac{h.x}{k}} \tag{4.2}$$

Where:

Nu - Nusselt Number
h - convective heat transfer coefficient; (W/m^2-K)
x - characteristic of the body under consideration-Length, L or Diameter, D; (m)
k - conductivity of the fluid; (W/m-K)

Prandtl Number: can be described to be a ratio reflecting the ratio of the rate that viscous forces penetrate the material to the rate that thermal energy penetrates the material.

$$\boxed{Pr = \frac{\mu.Cp}{k}} \tag{4.3}$$

Where:

Pr - Prandtl Number
μ - viscosity of the fluid; (N-s/m^2)
Cp - heat capacity of the fluid; (J/Kg-K)
k - conductivity of the fluid; (W/m-K)

Reynolds Number: represents a ratio of momentum to viscous forces. The flow becomes laminar if viscous forces dominate, and turbulent if momentum dominates.

$$\boxed{Re = \frac{\rho.u.x}{\mu}} \tag{4.4}$$

Where:

Re - Reynolds Number
ρ - density of the fluid; (kg/m^3)
u - flow velocity of the fluid; (m/s)
x - characteristic of the body under consideration-Length, L or Diameter, D; (m)
μ - viscosity of the fluid; (N-s/m^2)

Grashof Number: a parameter for free convection describing flow in the system. It represents the ratio of the buoyancy force to the viscous force acting on the fluid.

$$Gr = \frac{\rho^2.x^3.g.\Delta T.\beta}{\mu^2} \tag{4.5a}$$

$$\beta = -\frac{1}{\rho}\left(\frac{\delta\rho}{\delta T}\right)_T \tag{4.5b}$$

Where:

Gr	-	Grashof Number
ρ	-	density of the fluid; (kg/m^3)
x	-	characteristic of the body under consideration-Length, L or Diameter, D; (m)
g	-	acceleration due to gravity; (9.81 m/s^2)
ΔT	-	temperature difference between the solid surface and the fluid; (K or ^{o} C)
β	-	volumetric thermal expansion coefficient of the fluid; (1/K)
μ	-	viscosity of the fluid; (N-s/m^2)

The free convection heat transfer correlations are presented in this work for the no-flow simulations. Different methods to calculate heat transfer coefficients for the possible different geometries of the tank are elaborated in Appendix A.

Equations regarding heat transfer of crude oil through the storage tank are complex when solved analytically. To better understand solving of these equations numerically, knowledge in Computational fluid Dynamics (CFD) is required.

5 Computational Fluid Dynamics (CFD)

Computational fluid dynamics (CFD) is the branch of fluid mechanics that provides numerical approximation to the mathematical equations that govern fluid motion like predicting fluid flow, heat and transfer and chemical reactions. The fundamental equations governing the physical aspects of any fluid flow are the continuity, momentum, and energy (First Law of Thermodynamics) equations.

These are the mathematical statements of three fundamental physical principles:

i. Conservation of Mass

ii. Conservation of Momentum: Newton's second law (force = mass x acceleration)

iii. Conservation of Energy

These basic equations are either partial differential or integral equations in their most general form as shown in Equation (5.1). This equation is the conservative form of all flow equations for a two-dimensional system. Solving these equations analytically brings complexity.

$$\boxed{\frac{\partial(\rho\varphi)}{\partial t}+\frac{\partial(\rho u_x\varphi)}{\partial x}+\frac{\partial(\rho u_y\varphi)}{\partial y}=\frac{\partial}{\partial x}\left(\frac{\Gamma\partial\varphi}{\partial x}\right)-\frac{\partial}{\partial x}\left(\frac{\Gamma\partial\varphi}{\partial y}\right)+S_\varphi} \tag{5.1}$$

Where:
The transient term and convective term in x and y directions are on the left side of equation and the diffusive term in x and y directions and the source term are on the right side of equation.

ρ - density
u_x - x-velocity
u_y - y-velocity
Γ - diffusion coefficient
S_φ - source term

When φ equals 1, Equation (5.1) becomes a continuity equation. When φ is replaced by u and/or v Equation (5.1) becomes a conservation of momentum in x and y directions and it becomes a conservation of energy when replaced by T [18].

CFD replaces the integrals or the partial derivatives in these equations with discretized algebraic forms, which in turn are solved simultaneously to obtain numbers for the flow field values at discrete points in time and/or space [19]. The variables obtained throughout every point of the flow regime are velocity, pressure and temperature. From temperature and pressure; density, enthalpy, viscosity and thermal conductivity can be derived.

5.1 CFD Simulations Solving Procedures

The commercial general-purpose CFD programs available for example Star-CD, Fluent, CFX, FLOW-3D and Phoenics employ different solution techniques but same solving procedure. All CFD codes contain three main elements;

i. Pre-processor

ii. Processor (a flow solver)

iii. Post-processor

5.1.1 Pre-processor

This is the first stage that involves definition of all the relevant parameters required by the CFD code prior to the numerical solution of the equations. It is used input the problem geometry, generate the grid, define the flow parameter and the boundary conditions to the code [20].

Geometry Generation:

The body about which CFD simulations are to be carried out requires modeling. This generally involves modeling the geometry with a CAD software package. Usually the geometry of the system can be drawn in any CAD program and be imported. It is important to consider approximations of the geometry and simplifications to allow an analysis with reasonable effort. The extent of the finite flow domain in which the flow is to be simulated has to be decided.

This first step also involves boundaries definition. Definition of boundary conditions involves specifying the fluid behaviour and properties at all bounding surfaces of the fluid domain. In general, at any top, bottom, inlets, or outlets, the flow domain needs to be defined to set the appropriate boundary conditions. For transient problems, the initial conditions are defined. steady-state simulations also requires an initial guess to start the iterations [21].

Grid Generation (Meshing):

The physical domain is split into finite number of discrete regions or cells named mesh. The numerical solution is calculated in these mesh by solving the governing fluid flow equations inside. The mesh may be structured or unstructured, uniform or non-uniform, consisting of a combination of hexahedral, tetrahedral, pyramidal, prismatic or polyhedral elements. An accurate meshing is important for a successful simulation and accurate numerical solutions. The grid should exhibit some minimal grid quality as defined by orthogonality (especially at the boundaries), relative grid spacing or grid skewness.

For areas in the geometry where the physical properties to be predicted are suspected change rapidly a finer mesh may be used. The type of cell, the number of cell and the computation time can be optimized for accurate and reliable results. This optimization is defined as mesh convergence and can eliminate errors based on mesh structure [22].

Defining models:

After obtaining the computational mesh and boundary conditions, models regarding the simulation solution are defined. These models are tailored differently based on the physics of the problem. The type of flow to be encountered and whether heat transfer takes place or not should be defined. There is also an option for a user to write own models as a user-defined function [21].

Set Properties:

Once the physical models are selected, other physical problem parameters are then set. There are various properties of fluid available in ANYSYS Fluent which can be described as functions of composition, temperature and pressure. Example; density, viscosity, surface tension, heat conduction and diffusivity. Other properties including pressure, turbulence and turbulent viscosity depend on the flow.

All these physical properties of the fluids must be defined prior simulations. Some are already built into the CFD software or can easily found in available databases. Polynomials are also available to modify constants. Some properties can be calculated by writing a user-defined-function added to the CFD program [21].

5.1.2 Processor

This is a host of all mathematical techniques needed to approximate the differential equations governing the flow into numerical form, which can be solved by direct or iterative methods. It is done based on the conditions provided. Most of the CFD codes use iterative methods as they tend to be more robust, although can take longer to converge.

For the solver one can choose either a a coupled or segregated solver, pressure- or density based, and for transient problems you must choose either implicit or explicit time stepping methods. Also numerical schemes that enhance convergence, e.g. multigrid, upwind schemes or under-relaxation factors, must be defined or left at default. The quality of an acceptable solution in terms of the convergence criteria must also be defined [21].

5.1.3 Post-processor

The post-processor analyses the quality of the solution from the Fluent. Analysis of the final simulation results will give local information about flow or fluid etc. In post-processing, the numerical findings are displayed in a visual representation of the physical geometry (all or part of it) through which the fluid flows. It is also possible to superimpose the velocity, pressure and temperature distributions within the fluid [23].

6 Numerical Simulations

6.1 Geometry Generation

A three dimensional (3D) tank geometry is developed for this study. It is assumed to be in a half-full storage state.

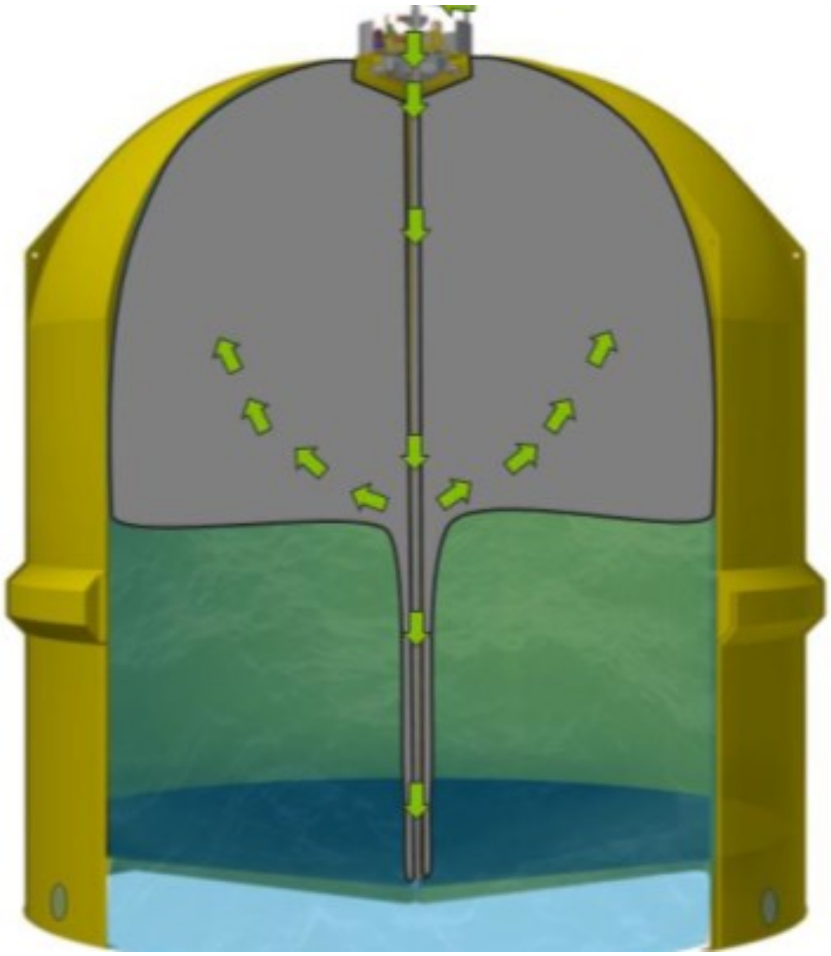

Figure 6.1: Half-full subsea storage tank [15]

The geometry consists of centre-pipe, flexible bag and a protective shell outside. This complex structure is generated from the real size (scale 1 : 1) of the tank as shown in Figure 6.2. It is developed by using ANSYS Workbench Design Modeler software.

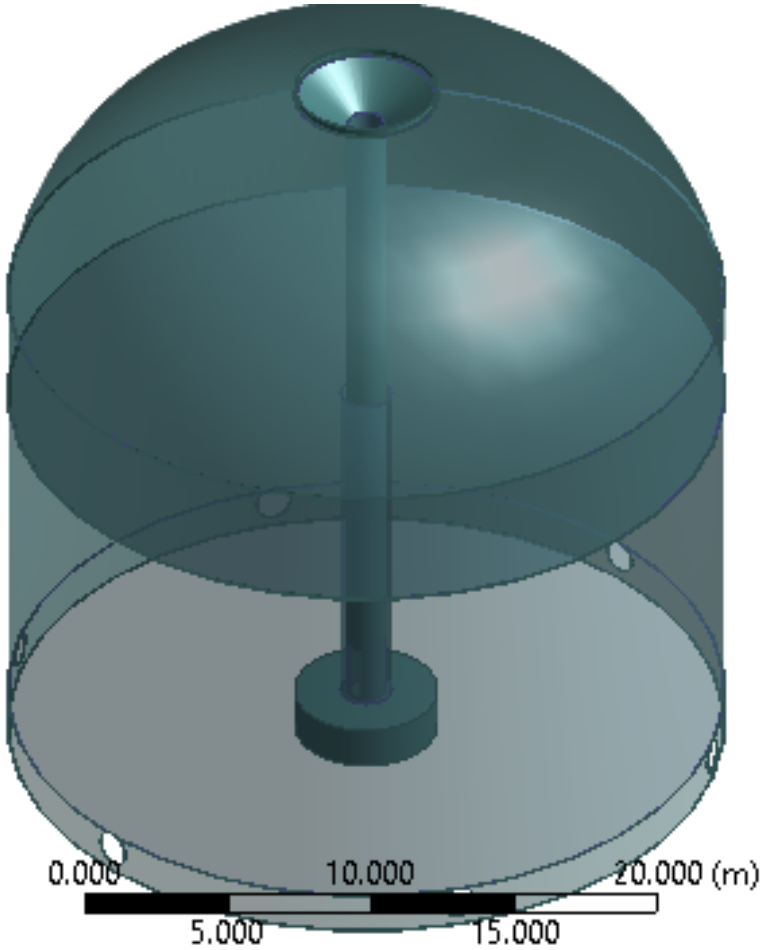

Figure 6.2: 3-D subsea storage tank geometry (side view)

A 3D examination of the model in two symmetry planes is considered sufficient in order minimize computational cost during simulations. Thus only one-sixteenth of the full geometry is taken for further processing (see Figure 6.3).

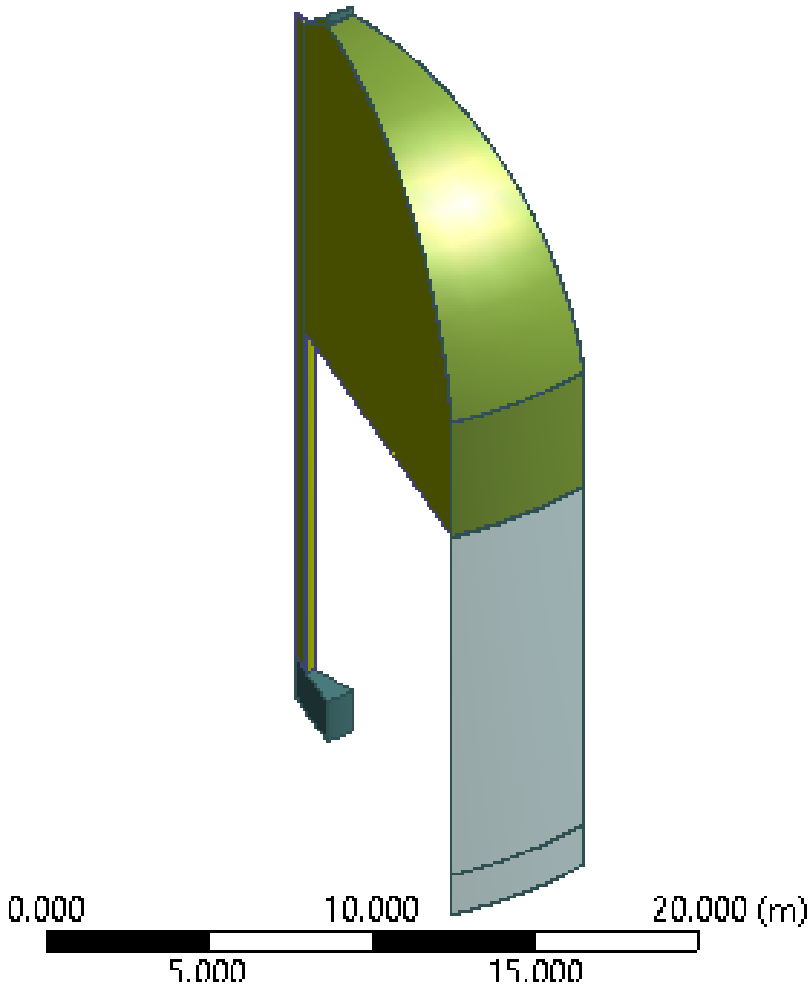

Figure 6.3: One-sixteenth of the full geometry indicating oil (yellow) in the pipe and bag (side view)

The case is further simplified by considering the fluid domain part of the geometry only. The centre-pipe is eliminated assuming there are negligible heat losses across the pipe walls. Thus, the flow in the annular section created between the bag and the pipe is omitted. Instead, the upward flow of oil into the bag starts from the bottom without the centre-pipe. A simpler case finally contains a model of the oil as shown in Figure 6.4.

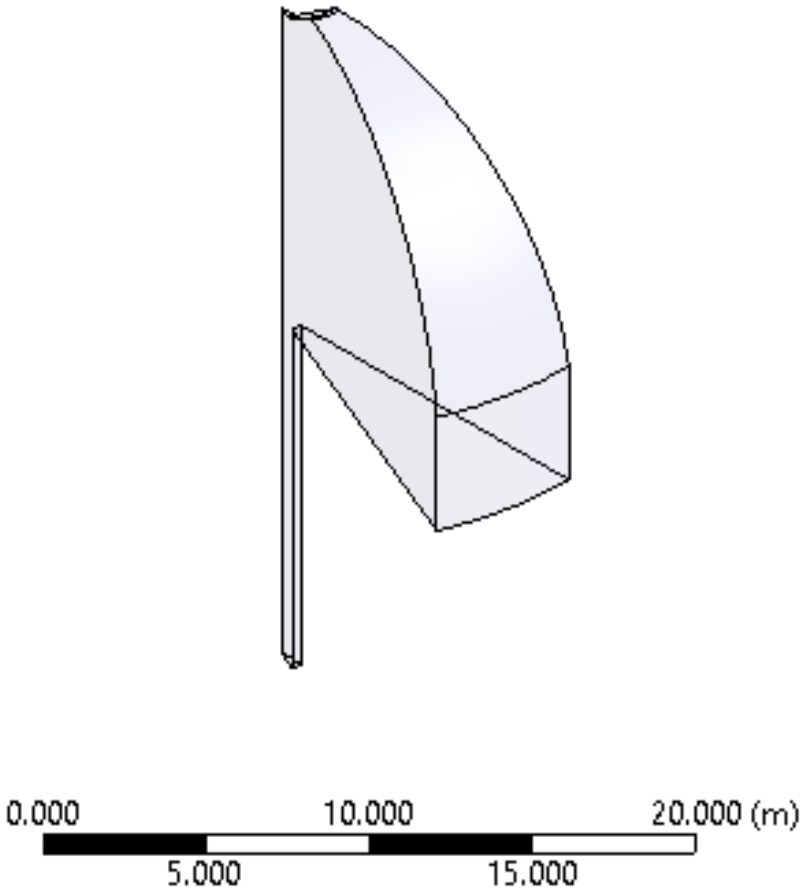

Figure 6.4: A fluid domain used for no-flow simulations in Fluent

6.2 Mesh Generation

ANSYS Workbench meshing software is used to generate mesh for the geometry. Each boundary in the geometry is labeled by creating named selections for the fluid domain and symmetry surface. Inlet and outlet boundaries are added for the flow simulations. Usually the outer wall boundaries are automatically detected in ANSYS Fluent.

In this study, it is necessary to name different outer wall boundaries to represent the protective structure and the part of the bag directly exposed to the seawater. This practice simplifies the assignment of the convective heat transfer coefficients which is a function of the structural configurations.

Figure 6.5: Initial Mesh of Fluid domain with 300 mm mesh size (symmetrical plane)

The body is initially meshed with elements of 300 mm size. The computational domain of this simulation consists of 3-D unstructured mesh to finely capture all the fluid-complex geometries. The number of elements generated from the 300 mm element size is 66324 and number of nodes generated is 98386.

6.3 Setting Simulations

After creating a computational mesh for the fluid geometry, a CFD analysis is set up in ANSYS Fluent for the flow and no-flow simulations. The initial-case for grid independence study consists of the 300 mm mesh. All simulations are set by referring to the guidance given in Fluent Tutorial Guide.

The most significant step before starting simulations in order to conduct more accurate solutions and stable numerical computation is to check the quality of the mesh. Mesh check and quality are performed to make sure that the minimum volume is not negative and the minimum orthogonality not to be below 0.01.

The pressure-based solver is selected to reduce computation time for the incompressible flows to be carried out. Physical models are tailored differently to fit for this study. In FLUENT, the conservation equations for mass and momentum are solved for all flows. For this thesis, both flow and no-flow include heat transfer so the software solves the energy conservation equation as well. Table 1 shows the physical equations used in simulations conducted in this thesis.

Table 1: Physical Models

Property	Action
Momentum	Automatically ON
Mass	Automatically ON
Energy	Turned ON
Viscous	Laminar

Zero water and zero gas contents are assumed to be present in the crude oil. Thus materials for the CFD simulation are set as crude-oil for fluid while solid materials are PVC/Nitrile-blend and GRP for the flexible bag and protective structure respectively.

The heat transfer process alters properties of the crude-oil. Therefore it is vital to define density and viscosity of oil as functions of temperature (T). Piecewise-polynomial function of temperature is used for the density and viscosity computations [24]. Table 2 displays the coefficients used in the function corresponding to Equation (6.1).

$$\boxed{\phi(T) = A_1 + A_2T + A_3T^2 + A_4T^3 + ...} \tag{6.1}$$

The specific heat capacity and thermal conductivity of the crude oil are maintained constant at 1980 J/kg-K and 0.12 W/m-K respectively.

Table 2: Inputs for Piecewise-Polynomial Functions [15]

Property (ϕ)	Coefficients						
	[A_1]	[A_2]	[A_3]	[A_4]	[A_5]	[A_6]	[A_7]
Viscosity	0.1561	-0.01242	6.179e-04	-1.881e-05	3.367e-07	-3.229e-09	1.271e-11
Density	844.23	-0.75					

The solid properties of the geometry used in the Fluent are showed in Table 3.

Table 3: Properties of Protective Structure and Bag [15]

Material	Density [kg/m^3]	Specific Heat Capacity [J/kg-K]	Thermal Conductivity [W/m-K]
GRP	2050	1060	0.6
PVC/Nitrile blend	1.025	1350	0.24

Boundary conditions for the flow simulations have an inlet and outlet additional to the no-flow boundary conditions. The flow is set to have a constant mass flow rate of 22.02 kg/s at the inlet. Heat loss is due to convection so it is necessary to specify the thermal properties of the materials with the ambient temperature (seawater temperature) at 0 ^oC.

Operating conditions for this study are 39.9e+05 Pa for pressure, 302.02 K for temperature and gravity which is enabled to be 9.81 m/s^2.

6.4 Solving

The default solution methods for running the simulations are retained default except for Pressure. PRESTO! is the discretization method selected as recommended for the Buoyancy-Driven flow problems, when using the pressure-based solver [25].

Standard Initialization is enabled with respect to the inlet conditions of pressure and temperature. Initialization starts at 29.02 ^oC and 39.9e+05 Pa. The plotting of residuals during the calculation is enabled to monitor convergence history. Report files and report plots for the average temperatures and velocity are created for post-processing purposes.

All calculations are run by altering the time step size from 1 sec to 3600 sec after every 100 time steps. Then simulations at 3600 sec are maintained to steady state. Time step sizes used are 1 sec, 10 sec, 100 sec, 1000 sec and 3600 sec.

A grid independence study involves cases of refining of the mesh from 300 mm to 100 mm to find the best mesh for all calculations that does not depend on mesh resolution. Table 4 shows the cases run in the grid independence study.

Table 4: No-Flow Cases Run by Refining Grid Size

Grid size	Case
100 mm	CASE A
200 mm	CASE B
300 mm	INITIAL-CASE

Simulations regarding sensitivity analysis of flow are carried out by modifying CASE D to 50% and -50% of the mass flow for more flow and less flow calculations respectively. Table 5 shows the cases run in the flow calculations.

Table 5: Flow Cases Run by Altering Flow

Mass Flow Rate	Case
11.01 kg/s	CASE C
22.02 kg/s	CASE D
33.03 kg/s	CASE E

7 Post Processing

Post processing of the simulations gives a complete insight into fluid dynamics results. It involves analysis and visualization of the results of the ANSYS Fluent CFD simulations. This is done in ANSYS CFD-Post. For this study, CFD-Post is mainly used to determine times and locations in the tank where temperature firstly reaches WAT under both flow and no-flow conditions. Locations with wax vulnerability when simulations are run to steady state are also determined in CFD-Post.

Contours of the fluid temperature and velocity along the symmetrical faces for Cases A, B and INITIAL-CASE at different flowtimes are displayed. Line 1 is inserted on the symmetrical face to track values of the local temperatures to sketch plots of temperature against distance in the axial direction.

Point X is located on the symmetrical plane near the bottom of the bag to capture values where temperature changes are significant and rapid. Values obtained at this point are used to analyze the best mesh for further simulations. Figure 7.1 shows the position of line 1 and Point X.

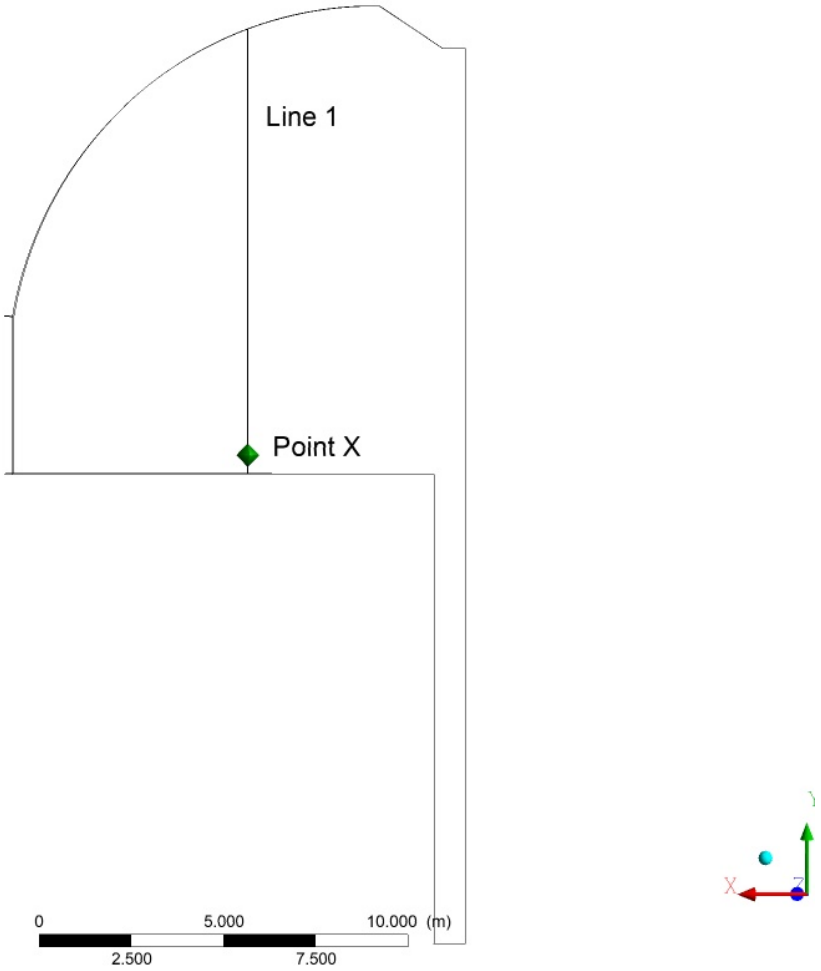

Figure 7.1: Symmetrical plane of the geometry showing the positions of Line 1 and Point X

Velocity vectors are also displayed to study the distribution of the velocity in the bulk fluid. Velocity vectors provide a good visualization of the flow around the module. They elaborate how efficient the convection process is. For both flow and no-flow calculations, velocity vectors are displayed to describe direction of the molecules and magnitude of the velocities .

8 Grid Independence Study

Grid independence study ensures that the CFD solutions are independent of grid resolution. The process starts with running simulations with coarse grid until a converged steady state of a certain measured property is reached. Then the initial mesh is further refined until the measured property stays within allowed tolerance [26]. An optimum mesh is the one that reduces simulation run time yet giving a mesh independent solution within accepted tolerance.

Prior to performing the CFD simulations in this thesis, a grid convergence study is conducted over three grid resolutions. Thus, three unstructured mesh sizes, from coarse to fine, are generated to ensure that the resulting solutions are sufficiently grid-independent. All solutions are supposed to be run to steady state and ensured not to produce unphysical quantities like negative absolute temperature.

The measured physical quantity used to obtain monitor points is fluid temperature near the bottom of the bag (Point X). Fluid temperature is monitored due to its physical relevance in wax appearance as stated previously, wax appearance is a function of temperature and composition. Point X is the location of interest as rapid temperature changes are observed near the bottom of the bag due to direct heat losses to the surrounding seawater. So once the temperature near the bottom of the bag is unchanging, the simulation is therefore considered grid-independent.

The initial mesh for this analysis is 300 mm. It is selected such that mesh check and quality performed ensured that the minimum volumes are not negative and the minimum orthogonality not below 0.01. Moreover, simulations are run until convergence is reached.

Further mesh refinement to 200 mm and 100 mm mesh is carried out until the solution stays within pre-defined acceptable error (in this study, +/-0.05% of finer grid solution is considered a sufficient tolerance). The relative error is calculated using equation 8.1.

$$\boxed{e = \left(\frac{T_i - T_f}{T_f}\right) \times 100\%} \tag{8.1}$$

Where:

- e - Relative error; (%)
- T_f - Fluid Temperature by fine mesh; (K)
- T_i - Fluid Temperature by given mesh; (K)

An optimal grid for further simulations is the one in which the computational cost is reduced without compromising with accuracy of the solution.

9 Results and Discussion

This study is aimed to investigate the cooling process and determine potential wax appearance locations in the subsea oil storage tank. FLUENT package program is used to solve all the natural and forced convection simulations. Grid Independence Study is first presented followed by no-flow simulations then flow simulations with flow effect on the results and finally sensitivity analysis. Shortcomings encountered are evaluated at the end of the chapter.

9.1 Grid Independence Study

A graph of the monitor points of fluid temperature against time steps as a result of cooling of the tank is plotted to check for a mesh independent solution. This is illustrated in Figure 9.1 where there are three results from the 2000 time steps simulations taken at Point X.

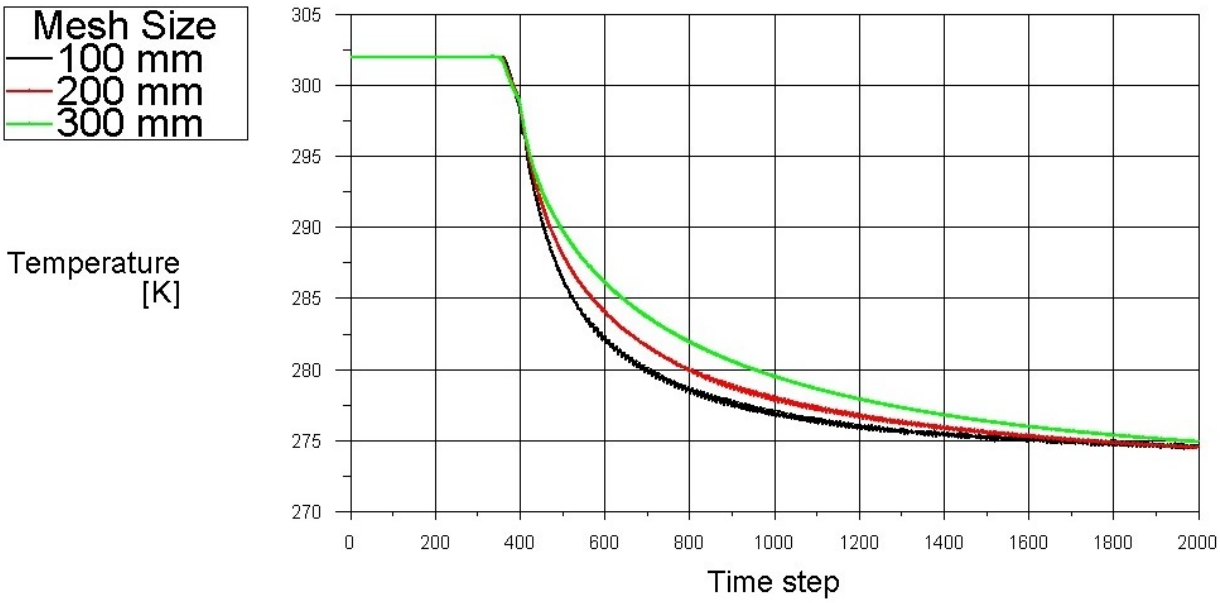

Figure 9.1: Fluid temperature variations at Point X using 300 mm, 200 mm and 100 mm mesh sizes for coarse, medium and fine mesh elements respectively

The plot of the solutions of the three test cases show that the solution is closer between medium and fine mesh compared to the coarse mesh. The deviations of values using coarse mesh from the finer mesh is due to the fact that too coarse mesh do not cover all effects that happen in a single element one by one, but rather covers multiple effects that then change as the mesh gets finer.

Quantification of the error between the three discrete solutions obtained from different mesh resolutions are reported in Table 6. The smaller mesh elements reduce errors based on mesh structure. Thus, +/-0.05% of the finer mesh is used as a grid convergence criteria since a 100 mm mesh provides extra accuracy. However, the extra accuracy gained is not worth the computational cost due to large number of simulations that must be performed.

Table 6: Summary of Fluid Temperature at Point X Showing Improved Accuracy as a Result of Refining Mesh

Mesh Size	Elements	Fluid Temperature [K]	Relative Error [%]
300 mm	66324	274.97	0.127
200 mm	168996	274.59	-0.011
100 mm	954108	274.62	0

Table 6 shows that with the coarse mesh, there is a jump in the value of interest that is not within the specified tolerance. The table quantifies the small change in solution between medium and fine mesh. -0.011% of 100 mm mesh is an acceptable accuracy as it remains within +/-0.05% of the finer mesh. The 200 mm mesh size is also the lowest grid available to ease simulation time without compromising with accuracy of the solution. Therefore, 200 mm mesh is considered an optimal mesh and will be used as a BASE-CASE for all the simulations. Figure 9.2 shows the final mesh used for further simulations.

Figure 9.2: Mesh with 200 mm grid size used for the CFD simulations (symmetrical plane)

9.2 No-flow Simulations

When the crude oil is at rest, Figure 9.8 shows that the average wall temperature is found to decrease with an increase in flow-time as the cooling process takes place. The solutions show that cooling starts at the bottom of the bag followed by the side and upper boundaries of the bag as.

Cooling is observed to start at the bottom of the bag since there is a direct contact between the bag and the seawater. The upper and side boundaries of the bag are in contact with the protective structure which provides resistance that slows down the cooling process of the walls.

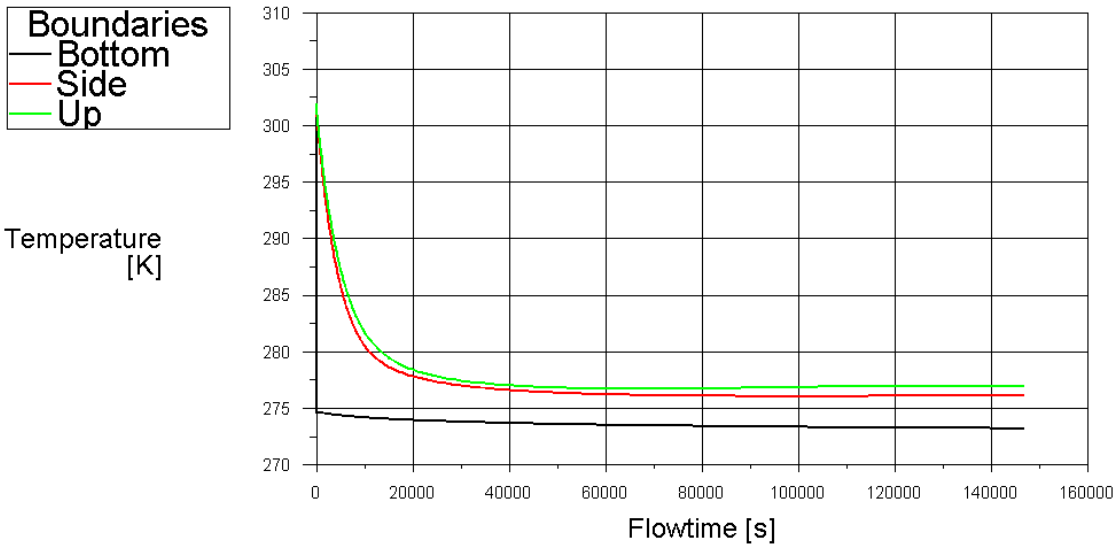

Figure 9.3: Average wall temperature profile showing cooling against flow-time for no-flow simulations

When cooling is allowed to take place for sometime, the wall temperature drops and reaches the WAT. Figure 9.4 presents temperature drops at different point surfaces at the bottom, side and upper walls to created to monitor results. When molecular diffusion is considered the main mechanism for wax deposition, a concentration gradient between the wax remaining in solution in the bulk fluid and amount of dissolved wax at the wall, causes diffused particles to be precipitated out of solution at the wall when WAT is reached.

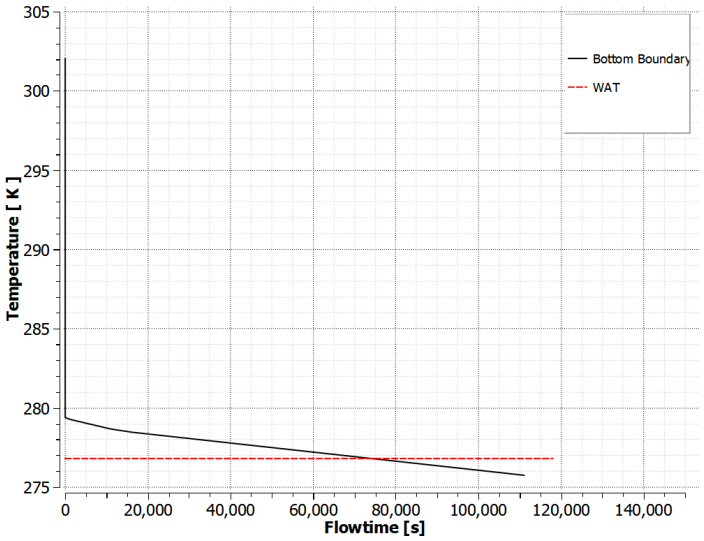

(a)

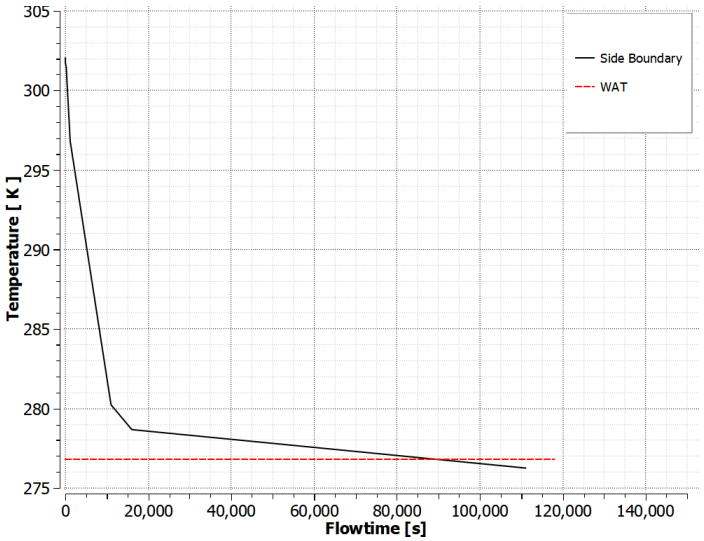

(b)

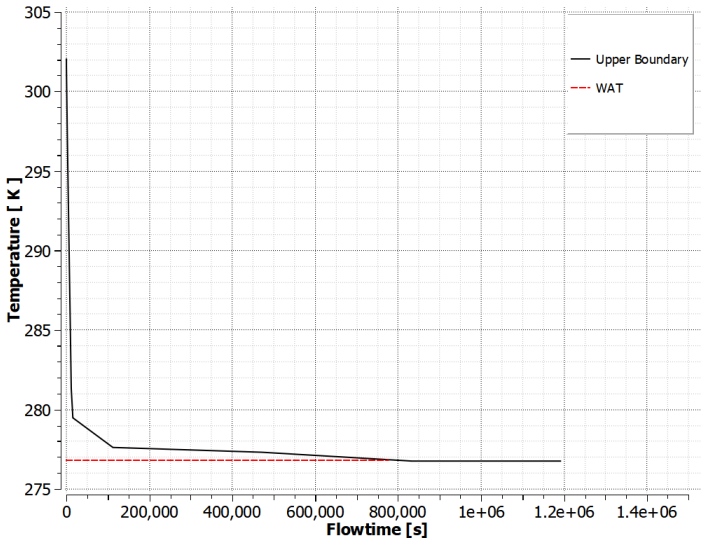

(c)

Figure 9.4: Point surface temperature against time for (a) bottom, (b) side and (c) upper boundaries as temperature reaches WAT for no-flow simulations

When the tank is allowed to cool for some time, the temperature of the wall reaches the surrounding temperature. Before cooling takes place in the oil, the bulk fluid temperature is seen to be uniform and higher than the temperature at the walls. The crude oil near the walls transfer internal energy to the environment before the crude oil at the center. As a result the bulk temperature of the crude oil in the center of the bag has a maximum value and decreases towards the walls due to heat loss to the seawater.

Figures 9.5 (a)-(d) present bulk temperature profiles at different flow-times. The difference between each profile is the decreasing rate of crude oil temperature. The figures show that cooling of oil starts at the walls towards the center of the bag. However a rapid temperature drop is observed near the bottom of the bag and in the outer pipe.

Due to less thermal resistance at the bottom of the bag since it is in direct contact to the seawater compared to the upper and side walls , the rapid temperature drop appears in the bulk fluid near the bottom of the bag and in the outer pipe. A small volume containing fluids in the pipe causes an early uniform fluid temperature drop from all sides. These are the potential areas which are vulnerable to wax appearance during the storage of crude oil.

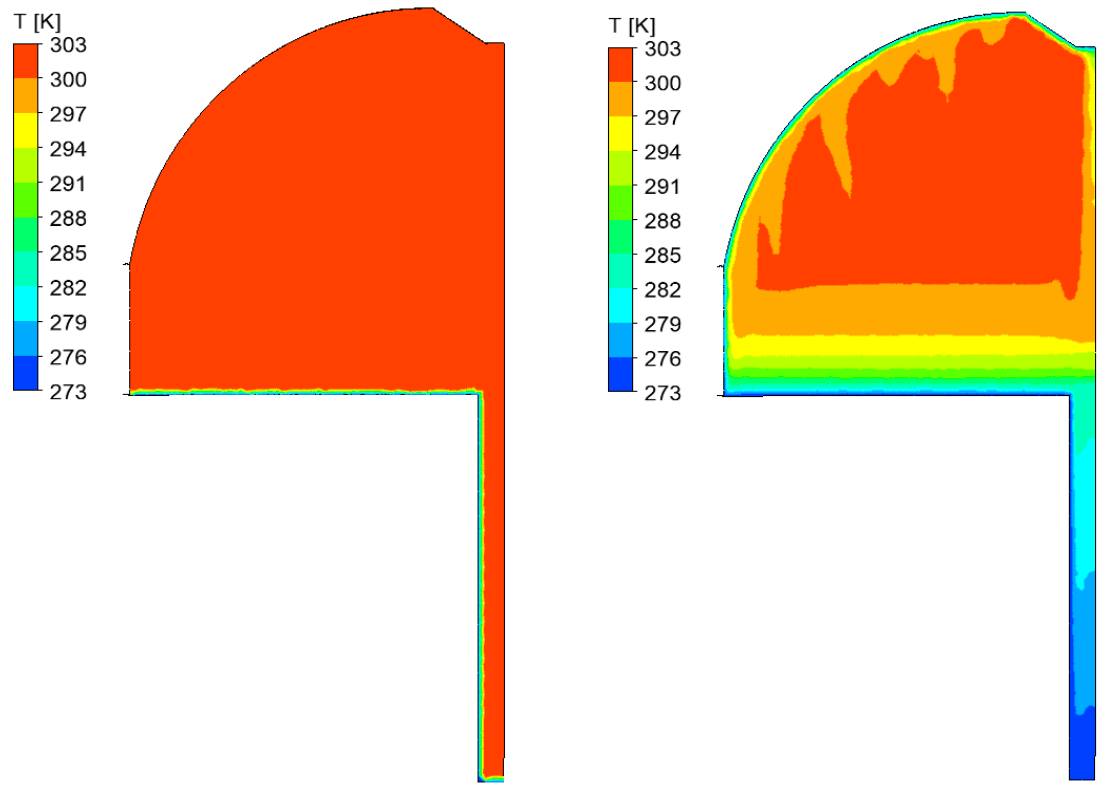

(a)

(b)

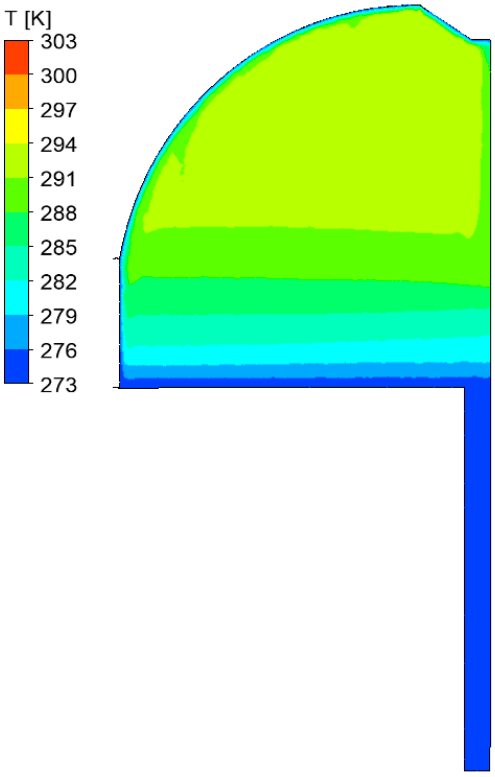

(c)

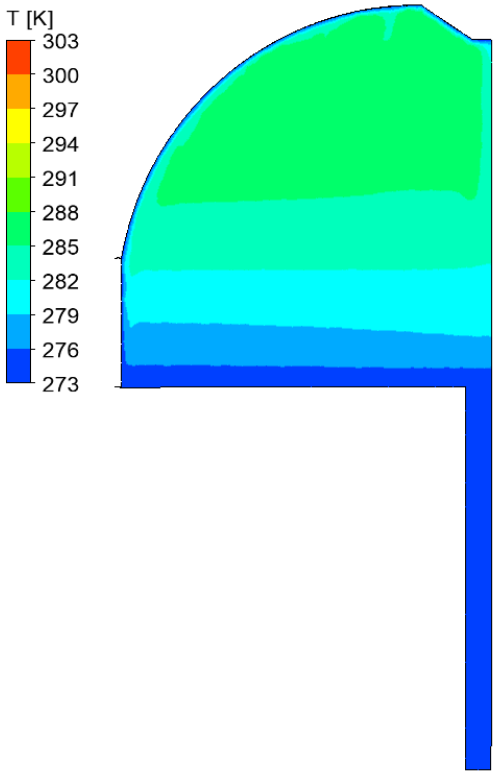

(d)

Figure 9.5: Bulk fluid temperature evolution at different flow-times during no-flow simulations (a) 100s (b) 471100s (c) 2271100s (d) 4071100s

9.2.1 Steady State Solution

Rapid temperature changes are observed near the bottom of the bag as illustrated earlier. In normal field operations, cooling of the bulk fluid would not take place to entirely reach the surrounding seawater temperature. Thus in this study, when the bulk fluid temperature near the bottom of the bag changes insignificantly with time then a steady state solution for no-flow simulations is considered to be reached.

Point X is a point surface located to monitor temperature near the bottom of the bag. Figure 9.6 shows a relatively uniform temperature near the bottom of the bag as cooling takes place.

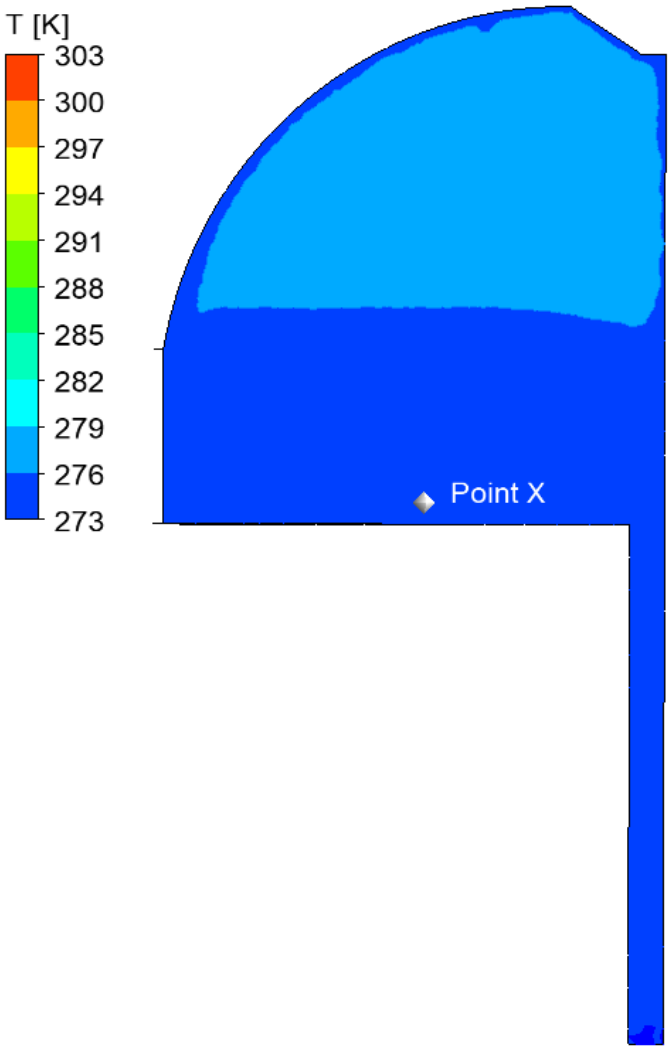

Figure 9.6: Bulk fluid temperature at the steady state solution

From the bulk fluid temperature distribution in Figure 9.6, it can be observed that a large region in the bottom and at the walls have the lowest temperatures below WAT. At the steady state, the temperature in the bulk fluid reaches the WAT at about 8.5 m from the bottom of the bag and 1.25 m from the top of the bag. These are the regions which are vulnerable to wax appearance provided the composition of oil remains constant.

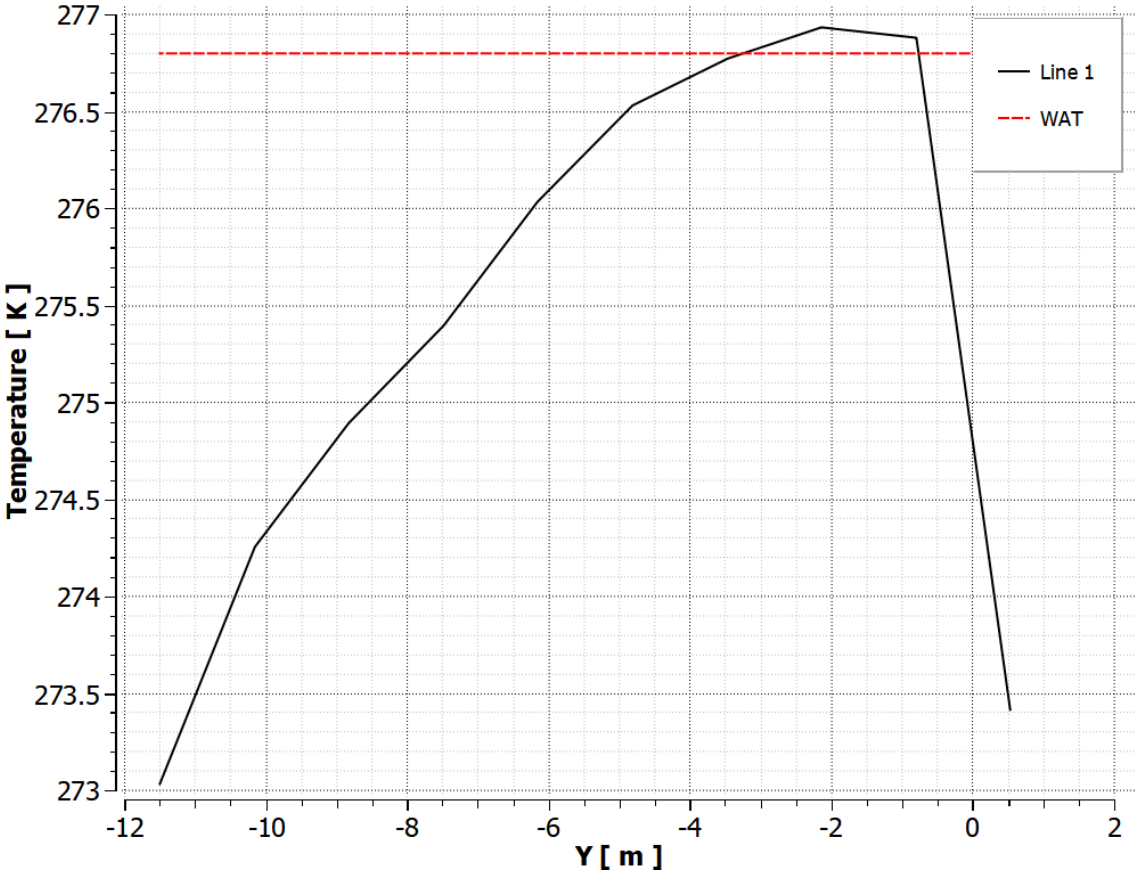

Figure 9.7: Bulk fluid temperature variations across line 1 when steady state is reached near the bottom of the bag in no-flow solution

9.3 Flow Simulations

Mass rate of 22.02 kg/s is introduced into the tank model to study how the results obtained when crude oil is at rest changes. There is no significant change in cooling of the walls of the tank when compared to no-flow simulations. Cooling is observed to start at the bottom of the bag followed by the side and upper walls.

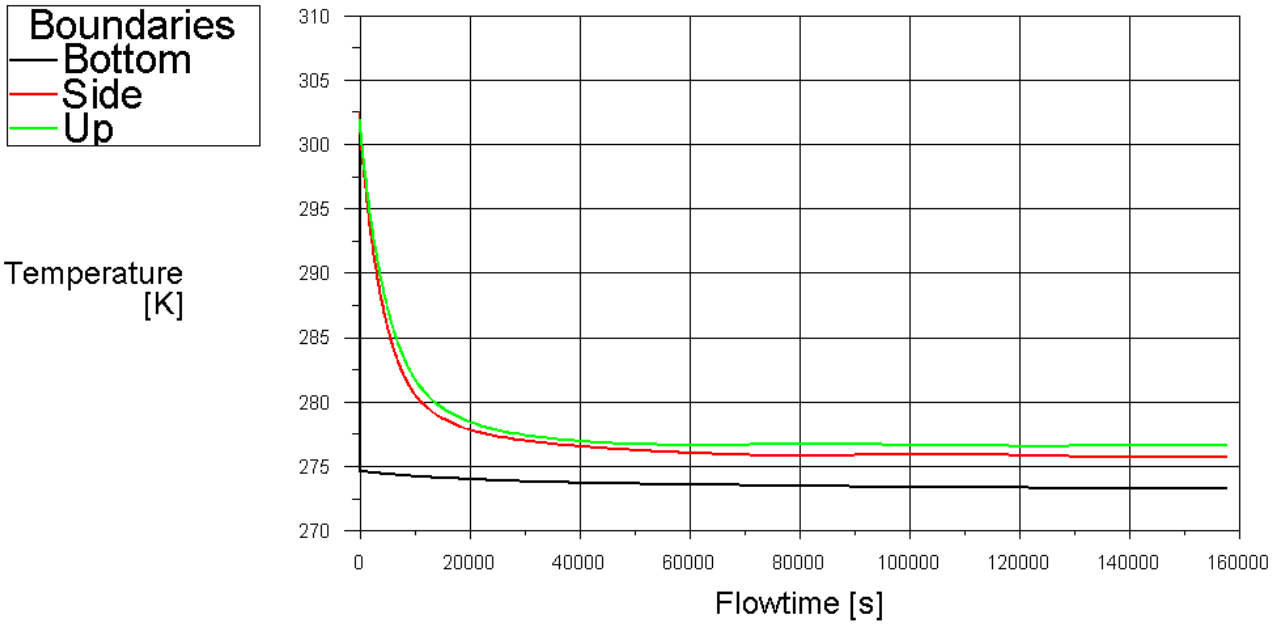

Figure 9.8: Average wall temperature profile showing cooling against flow-time for flow simulations

Bulk temperature in the bag during flow simulations is seen to drop more slowly compared to no-flow simulations. This is caused by a continuous inflow and outflow of hot fluids in the tank. Less heat is been lost to the surrounding seawater. Figure 9.9 shows bulk temperature profiles as the function of time.

Heat loss through the walls lowers the temperature of the oil nearby before the oil at the center. Temperature of the fluid at the center of the bag remains relatively near the initial fluid temperature. This temperature distribution makes it challenging for wax to move at the center of the bag since the Wax Disappearance Temperature (WDT) is 27 ^{o}C. Thus any wax appeared near the walls would not reach far into the fluid.

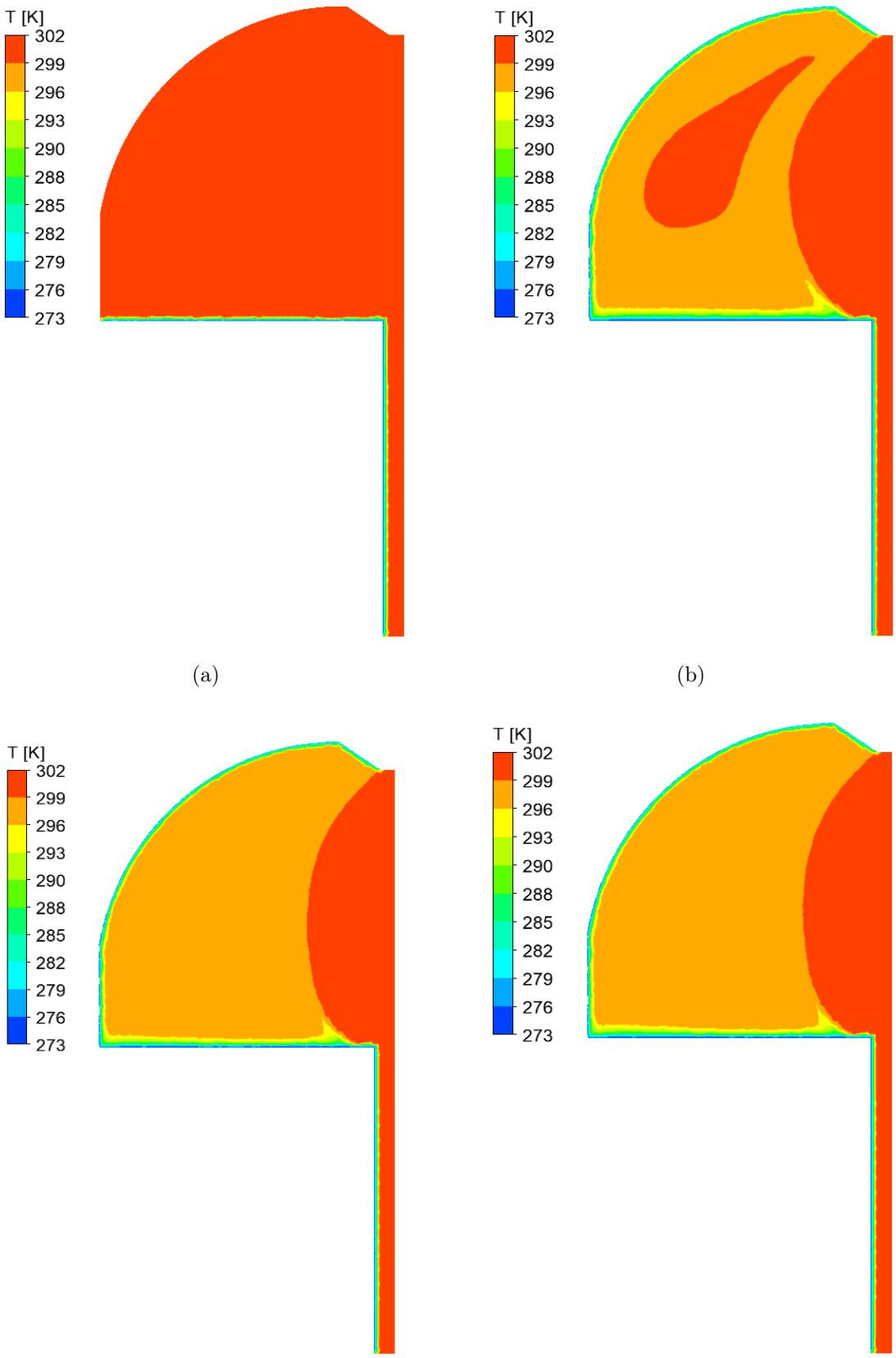

Figure 9.9: Bulk fluid temperature evolution at different flow-times during no-flow simulations (a) 100s (b) 471100s (c) 2271100s (d) 4071100s

An increase in the temperature of a bulk liquid caused by warmer oil flowing into the tank leads to an increase in the average speed of its molecules. Figure 9.10 illustrates how the continuous supply of warmer liquid causes the molecules to move faster at the inlet pipe and outlet of the tank thereby increasing the liquid's kinetic energy.

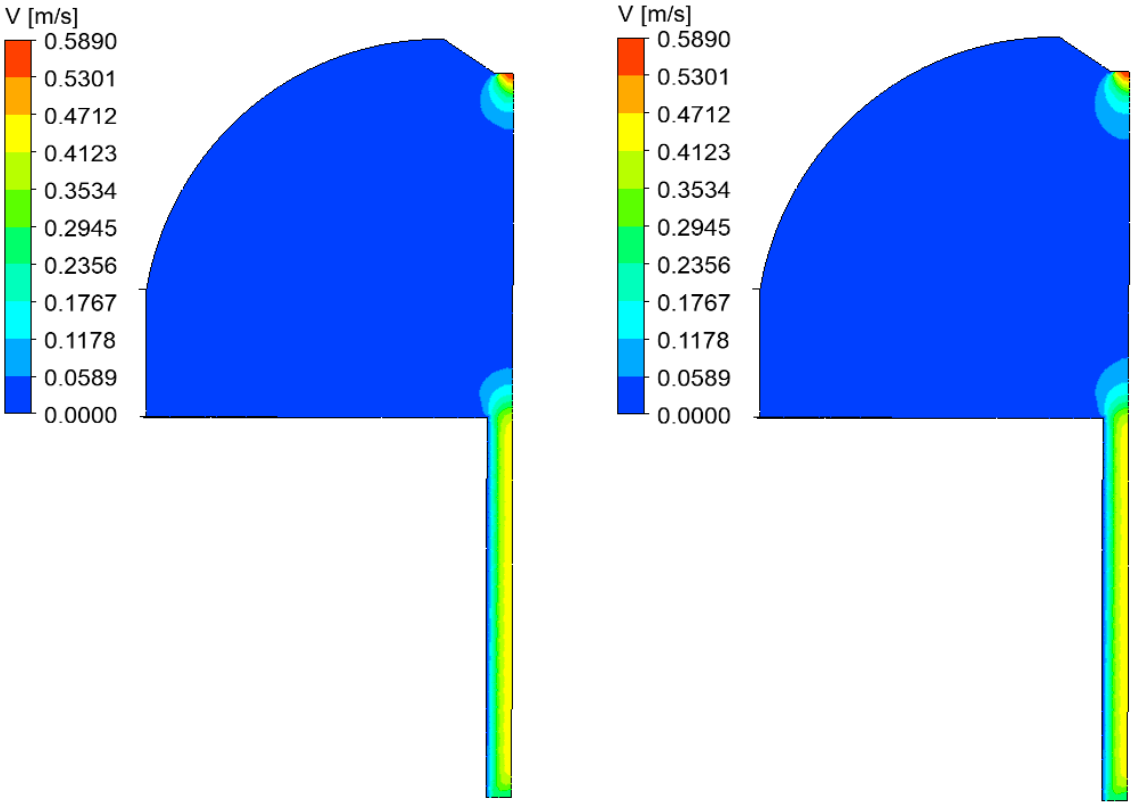

(a) (b)

Figure 9.10: Velocity contours at the beginning (a) and steady state (b) for flow simulations

Velocity vectors for the flow at the beginning and during steady state solutions are illustrated in Figure 9.11. At the beginning of the cooling process, the temperature of the bulk fluid remain fairly uniform at the initial temperature and the molecules are seen to move upwards towards the outlet. This is because of the inflow of molecules with temperature higher than the surrounding seawater. These warmer molecules are less dense and tend to flow upwards.

As cooling continues, the colder molecules become denser and starts to move downwards. In Figure 9.11 (b), the molecules in the center of the tank are warmer due to continuous inflow and outflow of the oil and hence move upwards. Molecules near the walls become denser due to cooling and thus tend to move downward.

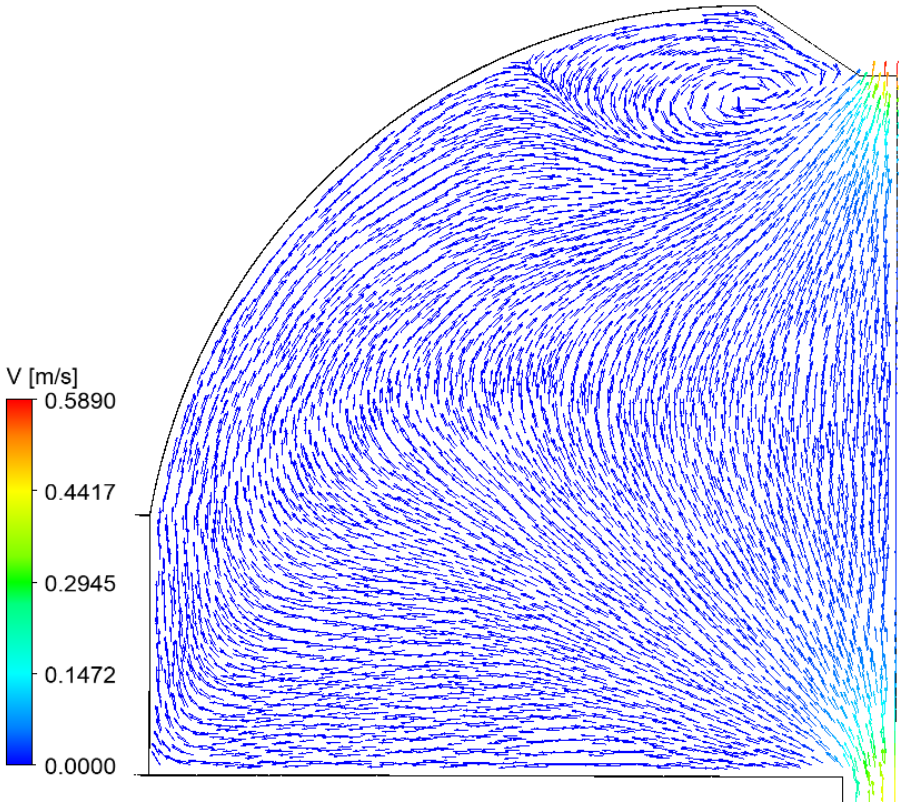

(a)

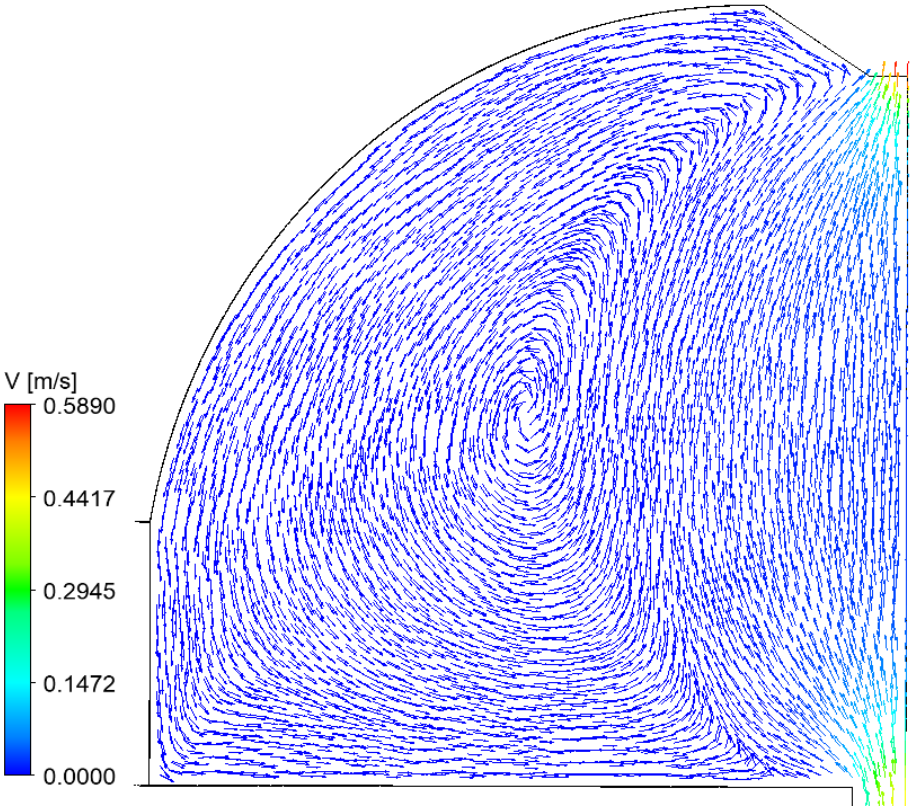

(b)

Figure 9.11: Velocity vectors at the beginning (a) and steady state (b) for flow simulations

9.4 Effect of Flow

When there is no flow, the decrease of crude oil temperature led to an increase in the oil viscosity which made the crude oil velocity drop substantially than in flow as can be seen in the velocity vector plot in Figure 9.12. No-flow simulations have less velocities than flow simulations.

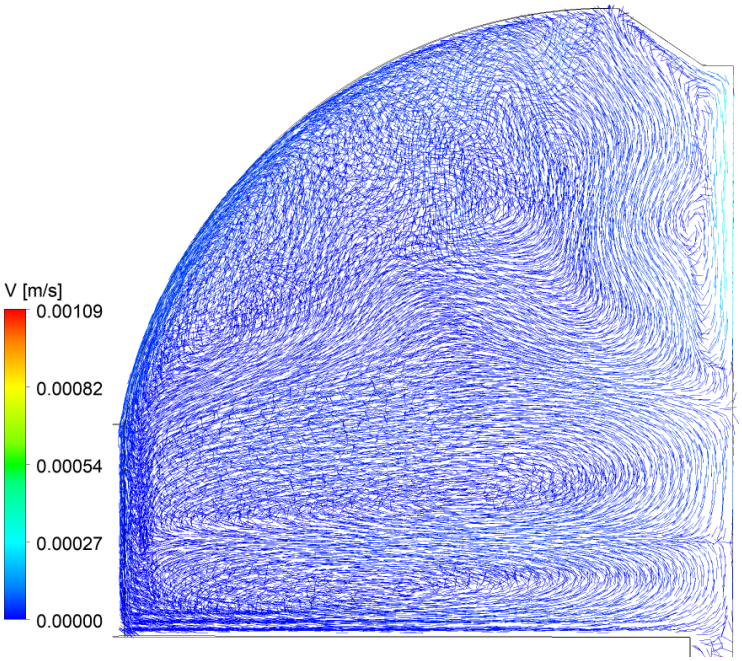

(a)

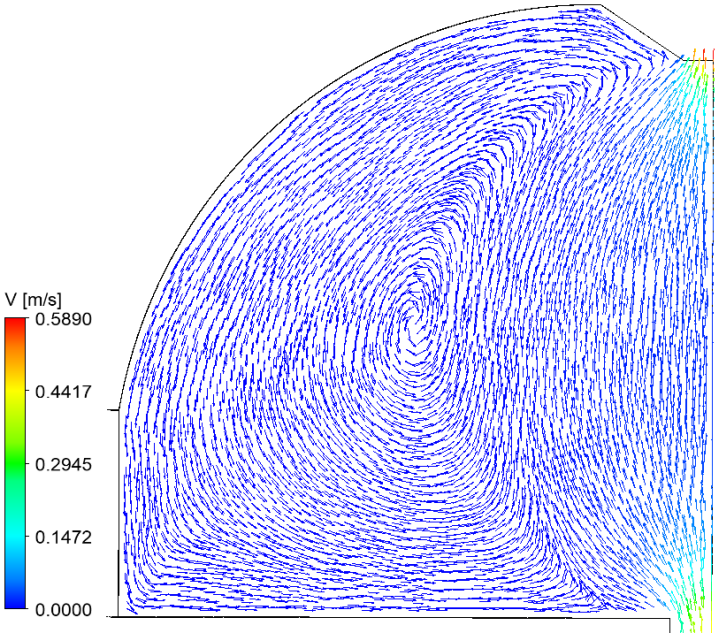

(b)

Figure 9.12: Velocity vectors at the steady state of flow simulations (4071100 s) for no-flow (a) and flow (b) solutions

Introduction of flow into the tank delays the process of heat transfer from the bulk fluid to the surrounding seawater. Figure 9.13 shows that cooling still takes place in the no-flow solution even though steady state is already reached for the flow solution. Bulk temperature is seen to drop rapidly starting from the bottom of the bag towards the center for the no-flow solution while temperature drop during flow starts at the walls almost uniformly.

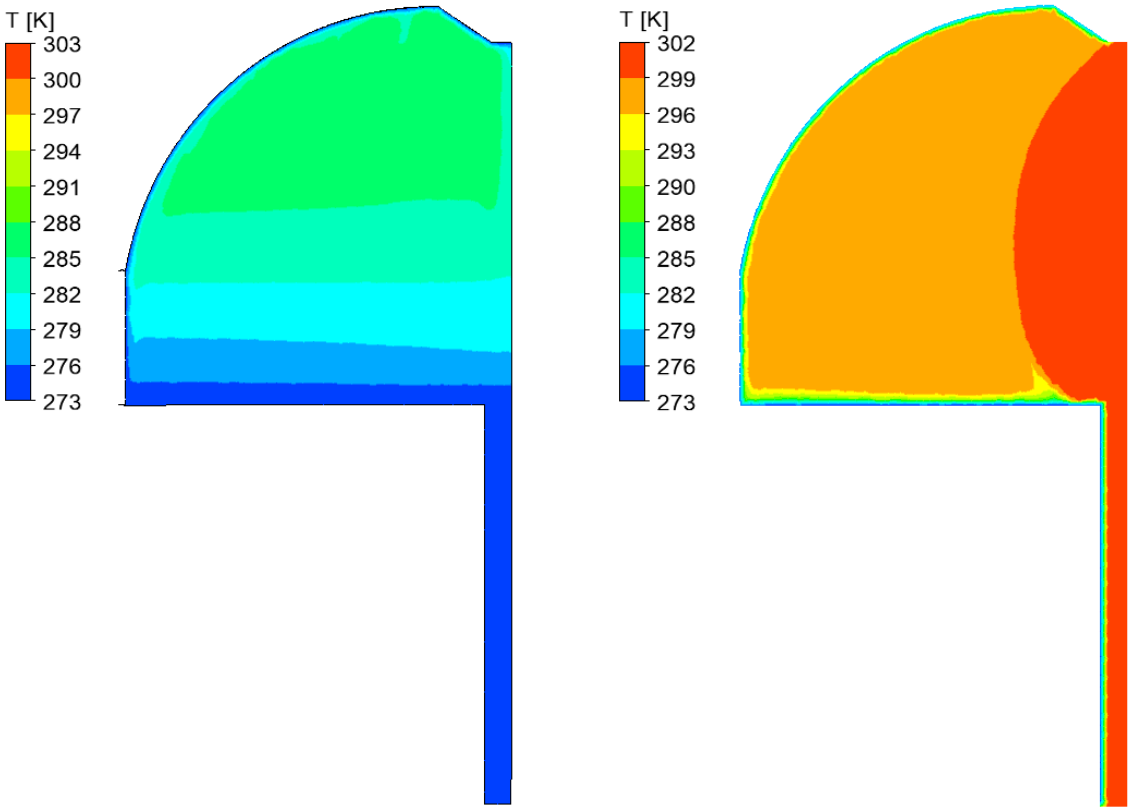

(a) (b)

Figure 9.13: Temperature profiles at the steady state of flow simulations (4071100 s) for no-flow (a) and flow (b) solutions

A large portion of bulk fluid in the no-flow simulations is seen to drop to WAT while for the flow simulations only fluid near walls drops to WAT. This indicates the likeliness of wax to appear in most parts when there is no flow of oil into the tank.

Due to this temperature distribution, there will be limitation of the areas in the flow solution where the bulk temperature can drop to WAT. For this study, it is found that when a flow of 22.02 kg/s in allowed into the tank, wax is likely not to appear at the upper boundary of the bag since temperature drop at the upper walls does not reach WAT. WAT is only reached at the bottom and side wall of the bag without affecting the bulk fluid in the center. The region of fluid reaching WAT for flow solution is approximately 1.5 m from the bottom.

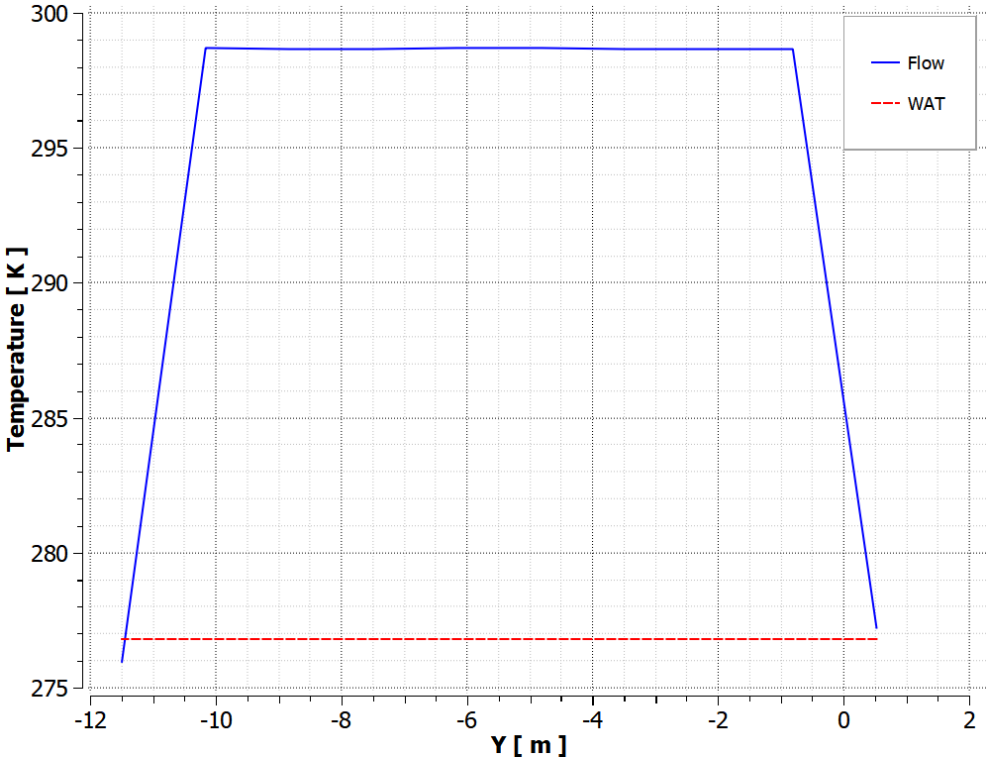

Figure 9.14: Bulk fluid temperature variations across line 1 when steady state is reached in flow solutions

9.5 Sensitivity Analysis

Sensitivity analysis was done to explore the effect of change of flow on the results. The cases were carried out by modifying the 22.02 kg/s to 50% and -50% of the mass flow. 11.01 kg/s and 33.03 kg/s were the rates for the reduced and increased flows respectively as refereed to the cases in Table 5.

The bulk fluid temperature is seen to drop faster when the flow rate is 11.01 kg/s and slowest with 33.03 kg/s. Figure 9.15 shows steady state temperature evolution at different flowrates. The region with warmer fluids (299 K to 302 K) at the center of the tank increases with the increase in flowrate. This is because velocities of warmer molecules in lower rates move slower than in the higher results resulting into poor replacement of the cooler molecules.

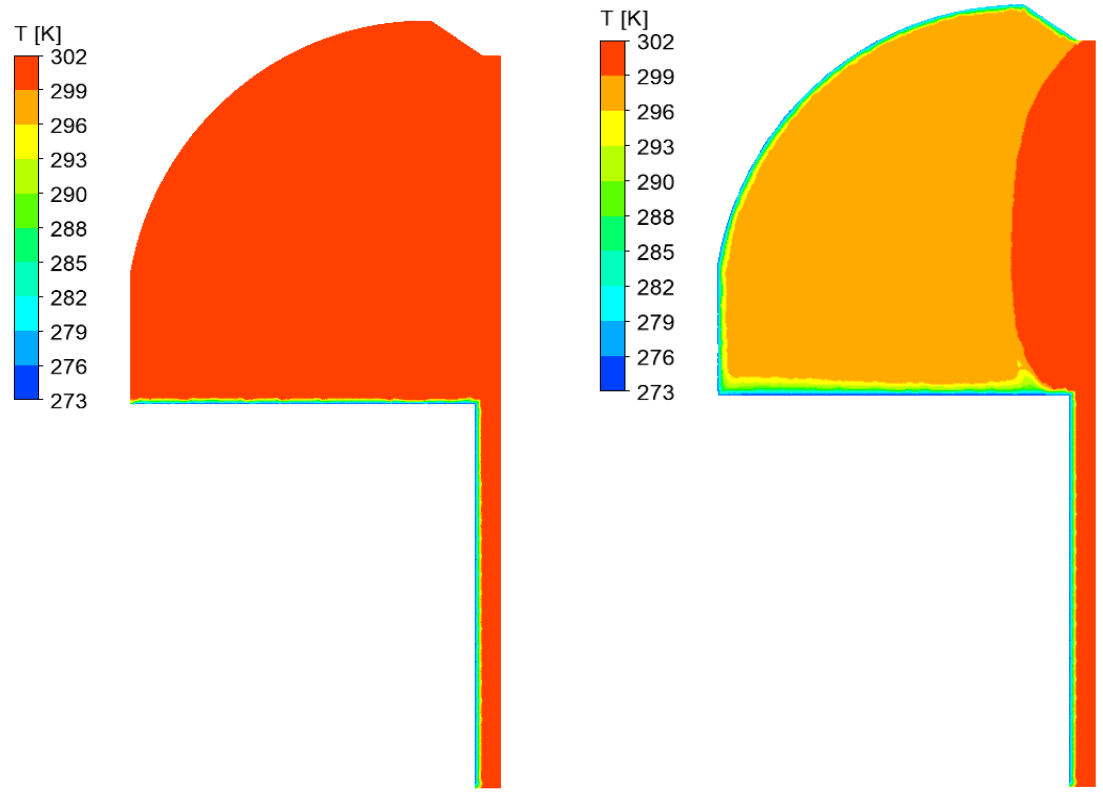

(a)

(b)

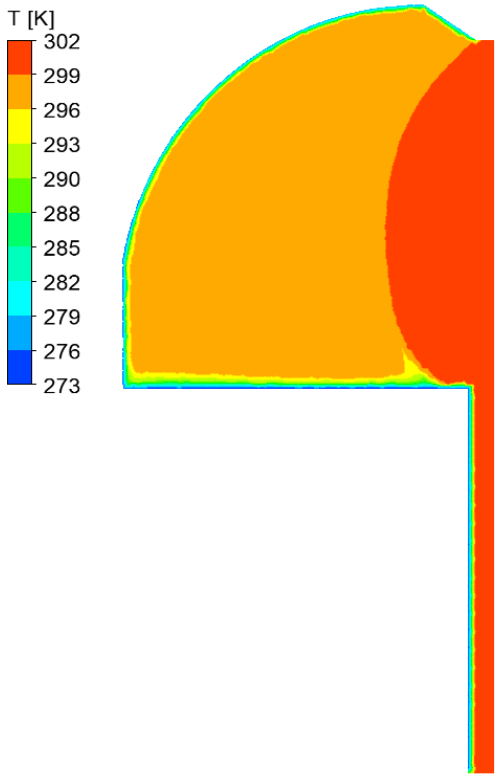

(c)

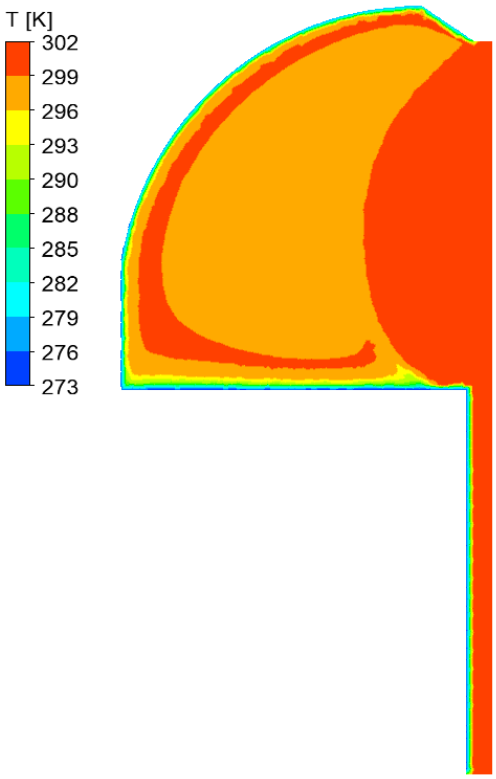

(d)

Figure 9.15: Temperature profiles at the beginning (a) and at the steady state of (b) 11.01 kg/s (c) 22.02 kg/s (d) 33.03 kg/s

The velocities are the lowest with 11.01 kg/s than in 22.02 kg/s and 33.03 kg/s. Figure 9.16 shows the upward movement of the warmer molecules and the downward movement of the cooler molecules due to density differences. The region of upward movement of the molecules is seen to increase with the flowrates. This leads to the higher temperatures in those regions.

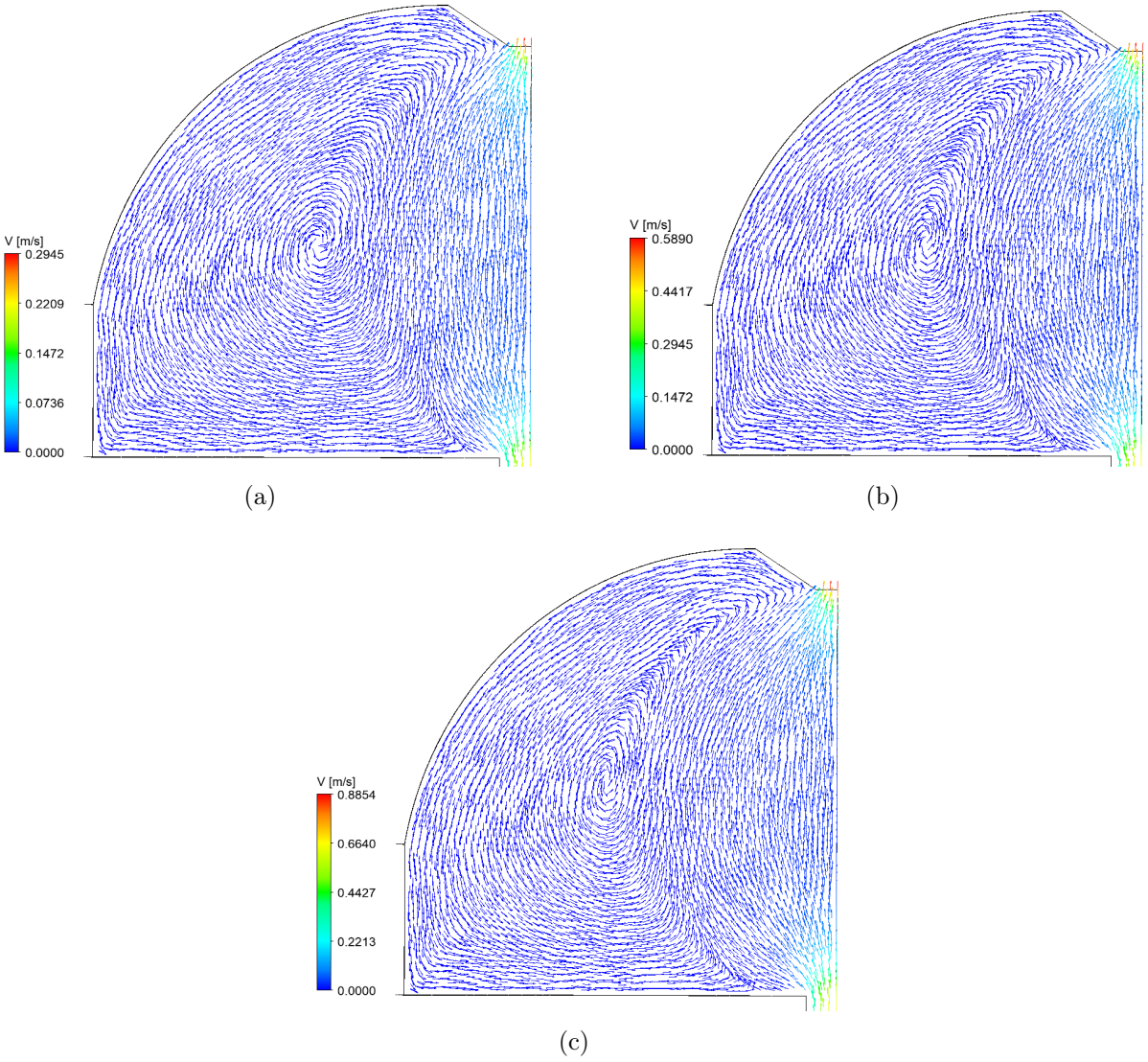

Figure 9.16: Velocity vectors at the steady state of flow simulations (4071100 s) for different flow rates. (a) 11.01 kg/s (b) 22.02 kg/s (c) 33.03 kg/s

Heat transfer from all the wall boundaries to the seawater is observed to be faster with the lowest flow rate than with the 22.02 kg/s and 33.03 kg/s as shown in Figure 9.17. This increases chances of wax to appear near the boundaries when flow rates are low. The wall boundaries for all the flow rates reach WAT except the upper boundary where WAT is only reached with lowest flow rate.

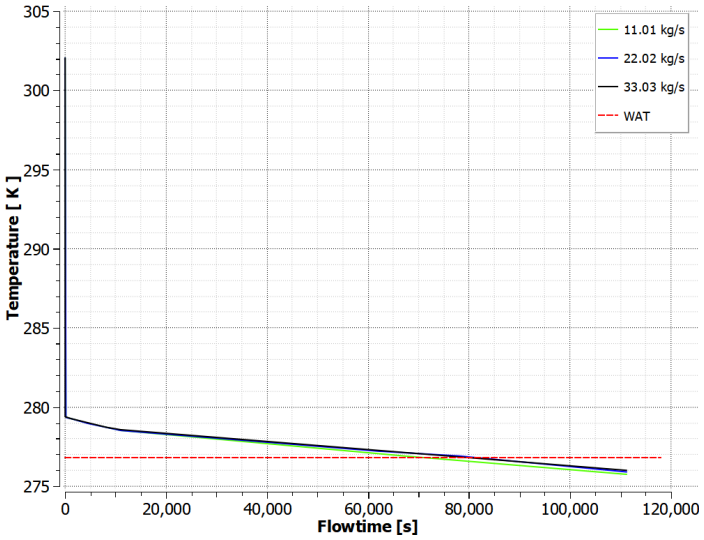

(a)

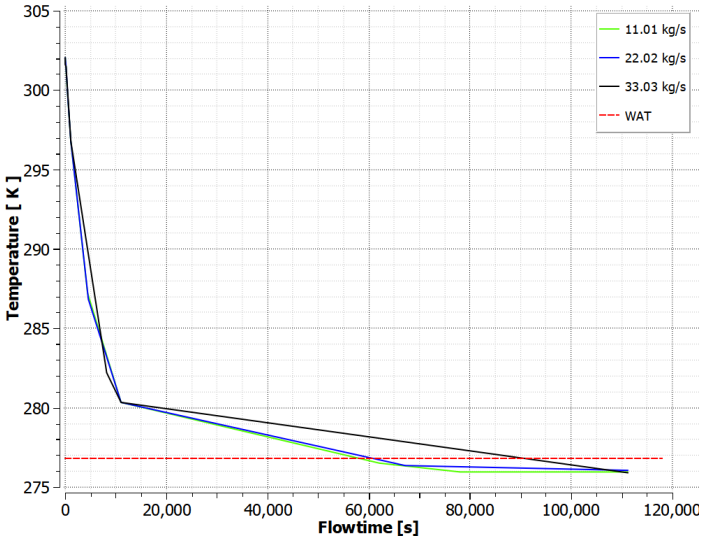

(b)

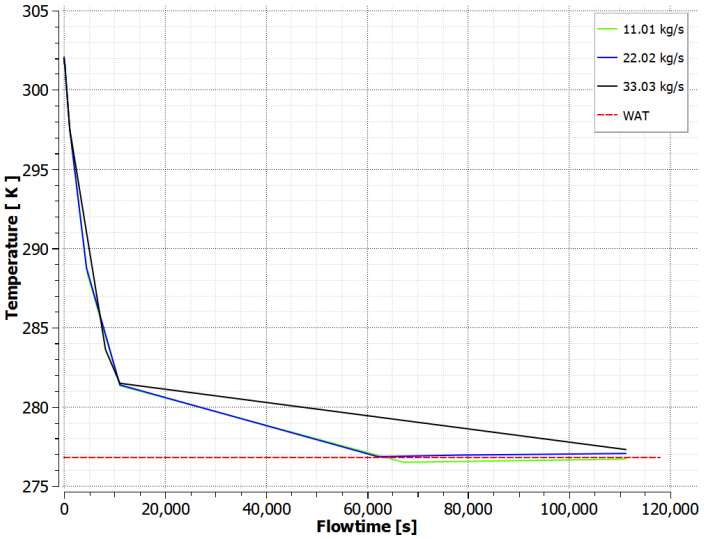

(c)

Figure 9.17: Wall temperature against time as it reaches WAT for (a) bottom, (b) side and (c) upper boundaries at flow rates of 11.01 kg/s, 22.02 kg/s and 33.03 kg/s

9.6 Shortcomings

The evaluation of the shortcomings encountered in this thesis is divided into shortcomings associated with the models and shortcomings in the conducted work.

9.6.1 Shortcomings in the Implemented Models

Simulations were done by assuming negligible heat transfer through the center pipe of the tank. The simplification of subsea tank geometry proceeded with the removal of the center pipe and assuming flow to only enter through the bottom of the outer pipe towards the bag and out through the top. However, heat transfer through the center pipe should be evaluated to study the effects on the results.

All flows were restricted to laminar flow conditions. Appropriate turbulent models should be selected for the flow simulations and the effect of those models on the results should be studied. For the boundary conditions, the bottom of the bag was assumed to be a stationary boundary. In the normal field operations, the boundary moves downwards to displace seawater as oil fills the bag. This effect should be taken into consideration in evaluating the fluid dynamics.

Another shortcoming present in the flow models, is the crude oil flow to be restricted to single phase. Oil flow in subsea is frequently accompanied by gas and water, however, neither of these phases were presented in the simulations. Presence of these phases might alter the composition of the crude oil as pressure and temperature change. The change in the composition of the crude oil has an effect on the wax appearance.

9.6.2 Shortcomings in the Conducted Work

Simulations started with time step size of 1 second. However, this time step size could not capture a realistic convection near the bottom boundary at the beginning of the simulations. Smaller time steps should be used at the beginning of the simulations even though this suggestion becomes computationally expensive.

Because of time constraints, only three cases of grid sizes were considered for the grid independence study. Future work could focus on collecting more data from different cases and seeing whether the same trend or pattern exists. Moreover, solutions of the monitor points should be run to steady state before the grid convergence criteria is applied. Experimental data or analytical models can be used to validate the numerical findings including locations vulnerable to wax appearance.

10 Summary

A simplification of the geometry to one-sixteenth (1/16) of the full subsea tank is obtained to save computation time. Further simplification involves removal of the center pipe assuming no heat is lost through the walls of the pipe and application of a stationary boundary at the bottom of the bag during inflow of oil into the tank.

Grid independence study is implemented to check for a mesh independent solution. Three cases of 300 mm, 200 mm and 100 mm mesh sizes for the coarse, medium and fine mesh respectively are evaluated. Based on the grid convergence criteria specified, a 200 mm mesh is the lowest grid available to ease simulation time without compromising with the accuracy of the solution.

A full implementation of the numerical simulations in Ansys FLUENT to predict time and locations which are vulnerable to wax appearance for both flow and no-flow conditions at constant crude oil composition are obtained. In all simulations, heat transfer through the bottom of the bag is faster compared to the side and upper boundaries of the tank thus becomes prone to wax appearance. This is due to the direct contact of the bag with the seawater. The outer shell provides thermal resistance hence delays cooling at the side and upper boundaries.

Rapid bulk fluid temperature changes are observed in the vicinity of the bottom of the bag during the no-flow simulations. The steady state solution is obtained when there are insignificant bulk temperature changes near the bottom of the bag. At the steady state, the temperature in the bulk fluid reaches WAT at about 8.5 m from the bottom of the bag and 1.25 m from the top of the bag. This region will be vulnerable to wax appearance if the crude oil composition remains constant.

A 22.02 kg/s flow is introduced in the model for the flow simulations. Based on the literature study, the warmer molecules become less dense and move upwards while the cooler molecules become dense and move downwards. The expectations are found to be true. Due to continuous inflow of the hot fluids, the velocity vectors at region in the center of the bag show that molecules moved upwards while the region near the walls have the molecules moving downwards due to cooling.

Sensitivity analysis is done to explore the effect of change of flow on the results. The simulation cases of 11.01 kg/s, 22.02 kg/s and 33.03 kg/s are performed for this purpose. It is observed that only with the lowest flow rate, the upper boundary of the tank reaches WAT. The low velocities in 11.01 kg/s slow down the molecular motions of the warmer molecules. Therefore cooling is more efficient compared to the higher rates. WAT for the side and bottom boundaries is reached faster for the 11.01 kg/s case compared to the 22.02

kg/s and 33.03 kg/s. There are minimal chances of wax to appear in the bulk fluid during flow conditions since even when a steady state solution is reached, the bulk temperature remains above the Wax Disappearance Temperature (WDT) which is 297 K for this study.

11 Future Work

A possible continuation of the current work is to introduce a moving boundary at the bottom of the bag. The normal operation of the tank requires that the bottom boundary moves downward to allow displacement of the seawater through the openings on the outer shell. Different moving velocities of the boundary can be applied to study fluid dynamics in the tank. As moving boundary tends to disturb wax deposition, appropriate models can be applied to evaluate wax thickness.

Usually crude oil flows with water and sometimes gas depending on the operating conditions. An extension of the current work, could be the applicability of the models to multiphase oil/water or gas/oil/water flow. These multiphase models can be used to capture the effect of the additional phases on wax appearance since an alternation on the composition of the crude oil as pressure and temperature changes affect wax appearance.

To further increase accuracy of the results, analytical models and experimental data can be used to validate the numerical findings. Also smaller time steps should be applied at the beginning of simulations even though it becomes computationally expensive.

References

[1] NOV. (n.d.). Subsea Storage Systems. 11306_ENG_v01, 1. Retrieved October 10, 2018, from http://nov.com/subsea.

[2] https://www.equinor.com/en/how-and-why.html#high-value-low-carbon.

[3] Owodunni, O. L., & Ajienka, J. A. (2007, January 1). Use of Thermal Insulation to Prevent Hydrate and Paraffin Wax Deposition. Society of Petroleum Engineers. doi:10.2118/111903-MS.

[4] Leontaritis, K. J., & Leontaritis, J. D. (2003, January 1). Cloud Point and Wax Deposition Measurement Techniques. Society of Petroleum Engineers. doi:10.2118/80267-MS.

[5] Sadeghazad, A., Christiansen, R. L., Sobhi, G. A., & Edalat, M. (2000, January 1). The Prediction of Cloud Point Temperature: In Wax Deposition. Society of Petroleum Engineers. doi:10.2118/64519-MS.

[6] Bacon, M. M., Romero-Zerón, L. B., & Chong, K. K. (2010, December 1). Determining Wax Type: Paraffin or Naphthene? Society of Petroleum Engineers. doi:10.2118/124799-PA.

[7] Singh, P., Fogler, H., & Nagarajan, N. (1999). Prediction of the wax content of the incipient wax-oil gel in a pipeline: An application of the controlled-stress rheometer. The Society of Rheology, Inc.

[8] Leontaritis, K. J. (1996). The Asphaltene and Wax Deposition Envelopes. Fuel Sci. Technol. Int. 14 (1-2): 13-39.http://dx.doi.org/10.1080/08843759608947560.

[9] Allen, T. O., & Roberts, A. P. (1982). Production Operations, second edition, Vol. 2. Tulsa, Oklahoma: Oil and Gas Consultants International.

[10] Molla, S., Magro, L., & Mostowfi, F. (2016, August 19). Microfluidic technique for measuring wax appearance temperature of reservoir fluids. The Royal Society of Chemistry 2016. doi:10.1039/c6lc00755d.

[11] Akhil, G. A., Mohammed Aiman Koya, K. P., Akhilesh, S., Muhammad Ashif, A. C., Khan, S., & Kanna, R. (2017). Determination of Cloud And Pour Point of Various Petroleum. International Refereed Journal of Engineering and Science (IRJES), 1.

[12] Huang, Z., Zheng, S., & Fogler, H. S. (2015). Wax Deposition: Experimental Characterizations, Theoretical Modeling, and Field Practices. 1st Edition.

[13] Burger, E. D., Perkins, T. K., & Striegler, J. H. (1981, June 1). Studies of Wax Deposition in the Trans Alaska Pipeline. Society of Petroleum Engineers. doi:10.2118/8788-PA.

[14] Kaalstad, J. P., & Kristoffersen, A. (2013, October 29). Flexible Subsea Storage Unit Development and Applications. Offshore Technology Conference. doi:10.4043/24537-MS.

[15] Equinor.

[16] Incropera, F.P., DeWitt, D.P, Bergman, T.L., & Lavine, A.S. (2007). Fundamentals of Heat and Mass Transfer, 6th Ed., Hoboken, NJ, John Wiley & Sons, .

[17] https://nptel.ac.in/courses/112108149/pdf/M6/Student_Slides_M6.pdf.

[18] Rukthong, W. (2014) Development of computational fluid dynamics program for flow inside crude oil pipeline. M.S. thesis, Department of Chemical Technology, Faculty of Science, Chulalongkorn University, Bangkok, Thailand.

[19] Anderson Jr, J. D. (1995). COMPUTATIONAL FLUID DYNAMICS: The Basics with Applications. McGraw-Hill.

[20] Ashgriz, N., & Mostaghimi, J. (2002). An Introduction to Computational Fluid Dynamics. In J. M. Saleh, & J. M. Saleh (Ed.), Fluid flow handbook. New York : McGraw-Hill.

[21] Andersson, B., Andersson, R., Håkansson, L., Mortensen, M., Sudiyo, R., & Wachem, B. v. (2012). Computational Fluid Dynamics for Engineers. New York, United States of America: Cambridge University Press.

[22] https://www.simscale.com/docs/content/simwiki/cfd/whatiscfd.html.

[23] Albaali, G., & Farid, M. M. (2006). Fundamentals Of Computational Fluid Dynamics.

[24] ANSYS Fluent 19.1 Theory Guide. ANSYS Inc.

[25] ANSYS Fluent 19.1 User's Guide. ANSYS Inc.

[26] https://www.computationalfluiddynamics.com.au/convergence-and-mesh-independent-study/.

[27] Lienhard IV, J. H., & Lienhard V, J. H. (2001). A HEAT TRANSFER TEXTBOOK (third edition ed.). U.S.A: J. H. Lienhard V.

Appendix

A Convenctive Heat Transfer Coefficient

The equations used to calculate the free convection heat transfer coefficients are derived from correlations of dimensionless numbers (See Equations 4.2, 4.3 and 4.5a) and sometimes the Rayleigh number (Equation A.1) [17]. Those equations are dependent upon flow conditions and geometry.

$$\boxed{Ra = Pr.Gr} \tag{A.1}$$

Where:

Ra - Rayleigh Number
Pr - Prandtl Number
Gr - Grashof Number

In this study, empirical correlations for the determination of heat transfer coefficients for common immersed (external flow) geometries are presented. Only correlations for horizontal plate, vertical cylinder and sphere configurations corresponding to the bottom, side and upper boundaries of the geometry respectively are used.

The general form of all correlations for natural convection heat transfer follows an average expression with constants, C and n:

$$\boxed{\overline{Nu} = \frac{\overline{h}.x}{k} = C.Ra^n} \tag{A.2}$$

Where: typically: n=1/4 and 1/3 for laminar flow and turbulent flows respectively.

A.1 Horizontal Plate

For heat transfer to the lower surface of a plate that is cooler than the fluid or from the upper surface of a plate hotter than the fluid (cases (b) and (c) respectively from Figure A.1), the equation becomes [16]:

$$\boxed{Nu_L = \begin{cases} 0.54.Ra_L^{\frac{1}{4}} & (10^4 \leq Ra \leq 10^7) \quad \text{(A.1.1a)} \\ 0.15.Ra_L^{\frac{1}{3}} & (10^7 \leq Ra \leq 10^{11}) \quad \text{(A.1.1b)} \end{cases}}$$

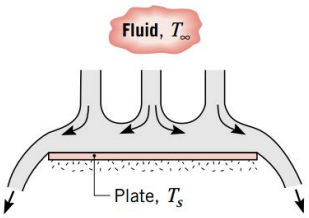

(a) Top surface of cold plate

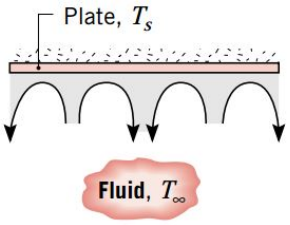

(b) Bottom surface of cold plate

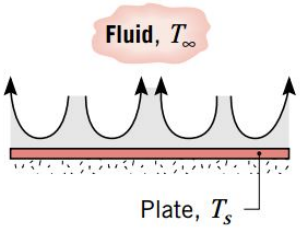

(c) Top surface of hot plate

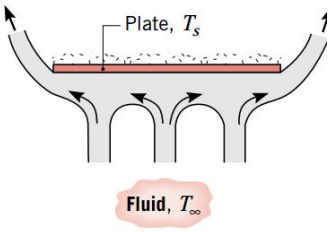

(d) Bottom surface of hot plate

Figure A.1: Buoyancy-driven flows on horizontal cold ($T_S < T_\infty$) and hot ($T_S > T_\infty$) plates. [16]

For heat transfer to the upper surface of a plate that is cooler than the fluid or from the lower surface of a plate hotter than the fluid (cases (a) and (d) respectively from Figure A.1), the equation becomes:

$$\boxed{Nu_L = 0.27.Ra_L^{\frac{1}{4}} \qquad (10^5 \leq Ra \leq 10^{10})} \tag{A.1.2}$$

The characteristic length, L_c can be altered to improve the accuracy of horizontal plate correlations for Nusselt Number:

$$\boxed{L_c \equiv \frac{A_s}{P}} \tag{A.1.3}$$

Where: A_s and P are surface area and perimeter of the plate respectively.

A.2 Vertical Cylinder

The heat transfer from the wall of the cylinder of height L, having its axis running vertically is the same as that for a vertical plate if the boundary layer thickness is much less than the cylinder diameter D. Here, the curvature effects can be neglected [27].

$$\boxed{\frac{L}{D} < 0.02(Gr^{\frac{1}{4}})} \tag{A.2.1}$$

Correlations to compute the average Nusselt number for free convection for a vertical plate may be applied on a vertical cylinder when a condition in Equation A.2.1 is satisfied (see Equation A.2.2a and A.2.2b) [16].

$$Nu_L = \begin{cases} \left[0.825 + \dfrac{0.387.Ra_L^{\frac{1}{6}}}{[1+(\frac{0.492}{Pr})^{\frac{9}{16}}]^{\frac{8}{27}}}\right]^2 & \text{for all values of Ra:} \quad \text{(A.2.2a)} \\ 0.680 + \dfrac{0.670.Ra_L^{\frac{1}{4}}}{[1+(\frac{0.492}{Pr})^{\frac{9}{16}}]^{\frac{4}{9}}} & \text{for laminar flow (Ra} \leq 10^9\text{)} \quad \text{(A.2.2b)} \end{cases}$$

where Equation A.2.2b is suggested to be slightly better for laminar flow.

However when the boundary layer is thicker, then heat transfer will be enhanced by the curvature therefore corrections to the vertical plate results need to be done using Figure A.2.

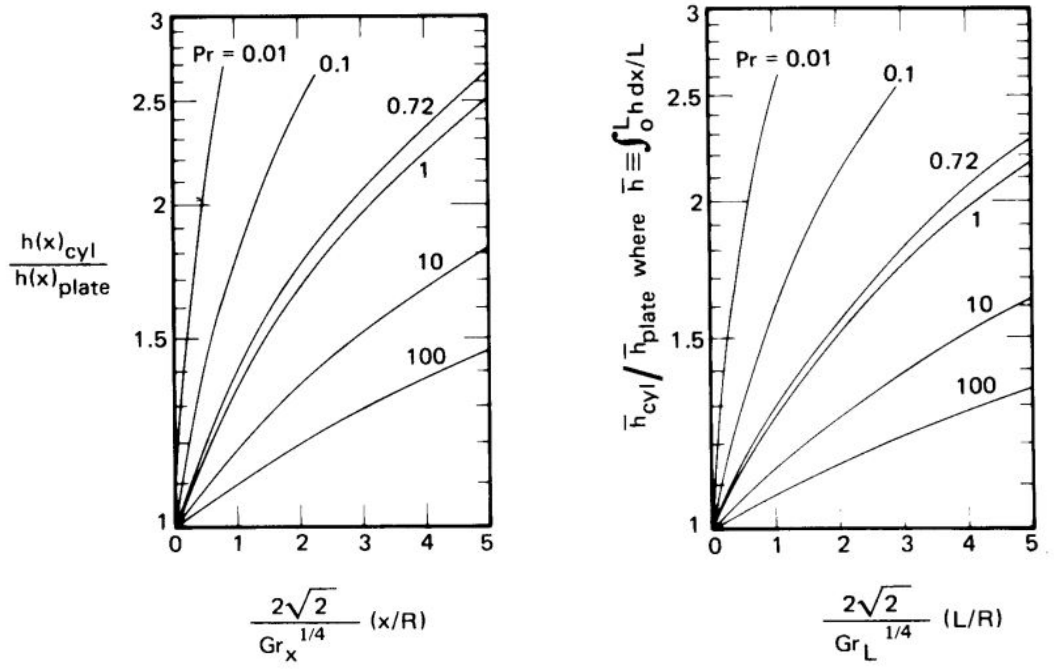

(a) Correction for h at x

(b) Correction for average h

Figure A.2: Corrections for h and $\overline{h}$ on vertical isothermal plates to be applicable for vertical isothermal cylinders [27].

A.3 Sphere

Sphere has a clearly specifiable value, 2 of Nu as Ra $\rightarrow$ 0. At this point when buoyancy forces reach zero might be due to low gravity, a very small value of β, very high viscosity or small diameter. Then heat will only be lost by conduction [27].

$$\boxed{Nu_D = 2 + \frac{0.589.Ra_D^{\frac{1}{4}}}{[1 + (\frac{0.492}{Pr})^{\frac{9}{16}}]^{\frac{4}{9}}}} \tag{A.3.1}$$

Equation A.3.1 is recommended for spheres in fluids of Pr$\geq$ 0.7 and Ra$_D$ $\leq 10^{11}$ [16].

B Convective Heat Transfer Coefficient Calculations

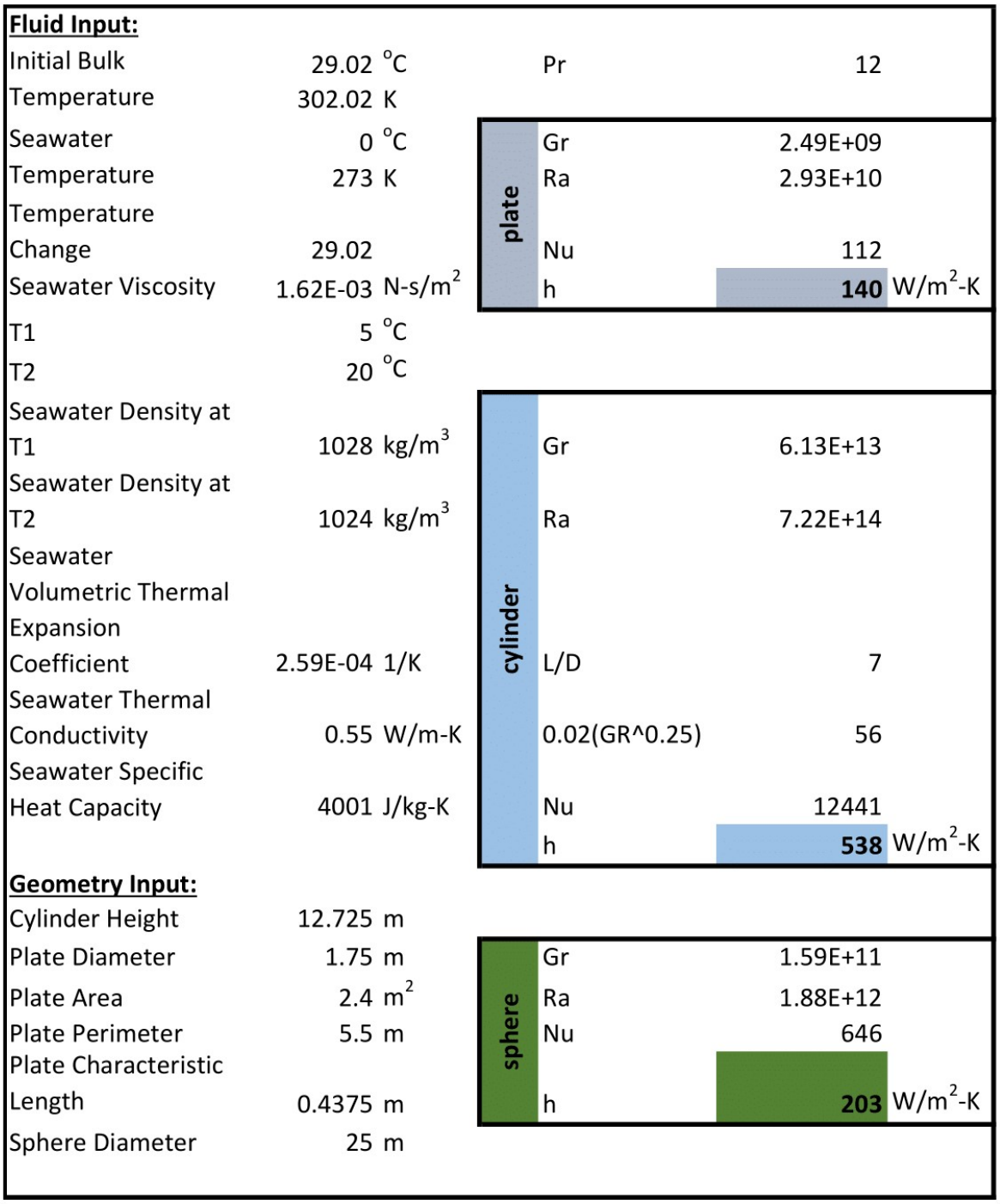

Fluid Input:						
Initial Bulk Temperature	29.02	°C		Pr	12	
	302.02	K				
Seawater Temperature	0	°C	plate	Gr	2.49E+09	
	273	K		Ra	2.93E+10	
Temperature Change	29.02			Nu	112	
Seawater Viscosity	1.62E-03	N-s/m^2		h	**140**	W/m^2-K
T1	5	°C				
T2	20	°C				
Seawater Density at T1	1028	kg/m^3	cylinder	Gr	6.13E+13	
Seawater Density at T2	1024	kg/m^3		Ra	7.22E+14	
Seawater Volumetric Thermal Expansion Coefficient	2.59E-04	1/K		L/D	7	
Seawater Thermal Conductivity	0.55	W/m-K		0.02(GR^0.25)	56	
Seawater Specific Heat Capacity	4001	J/kg-K		Nu	12441	
				h	**538**	W/m^2-K
Geometry Input:						
Cylinder Height	12.725	m				
Plate Diameter	1.75	m	sphere	Gr	1.59E+11	
Plate Area	2.4	m^2		Ra	1.88E+12	
Plate Perimeter	5.5	m		Nu	646	
Plate Characteristic Length	0.4375	m		h	**203**	W/m^2-K
Sphere Diameter	25	m				

Figure B.1: External natural convective heat transfer coefficients for the wall woundaries

C Step-by-step FLUENT

i. Launch ANSYS Workbench

ii. Drag Fluid Flow (FLUENT) into the blank work area

iii. Mark Geometry. Choose 3D as analysis type under Advanced Geometry Options in the right hand box. Then double-click on Geometry.

iv. Select desired units and create the full geometry of the subsea tank. Follow the User Guide in how to do this (ANSYS Inc 2019c).

v. Apply two symmetry planes to reduce the full geometry to 1/16.

vi. Update program in ANSYS Workbench. Launch Mesh.

vii. Create mesh, follow instructions given in User Guide (ANSYS Inc 2019c). Then create named selections, such as Upper, side and bottom wall boundaries, symmetry and fluid. Add inlet and outlet for the mesh to be used in flow simulations.

viii. Update program in ANSYS Workbench. Launch Setup. A pop-up window will then emerge, set the required characteristics according to the specific problem. Normally, double-precision is used.

ix. A separate setup window will emerge. Follow the suggested procedure indicated by FLUENT to define all relevant information. Section 6.3 explains all the relevant setting like defining models, material etc. done in this study.

x. After setting up all parameters, set values for the solution convergence if necessary. Otherwise, continue to define a reference surface for the calculation, usually the inlet for the case of flow into the tank.

xi. Select either standard or hybrid initialization. Then initialize project.

xii. Select autosave mode of writing the files for easy analysis.

xiii. Run Calculation. Define time step size and number of time steps. For this project, time step size was changed from 1 sec, 10 sec, 100 sec, 1000 sec and finally 3600 sec after every 100 time steps.

xiv. After the solution has converged. Save project and exit the setup window.

xv. Launch Results from ANSYS Workbench, a separate window will emerge. Follow the CFD-Post User Guide's instructions on how to set up the results for the parameters in question. For this study contours of fluid temperature and velocity were important for analysi. Export the charts to Excel.

D Fluid Properties Used in FLUENT

This section presents plots of density and viscosity of crude oil from Equinor. Since these properties change with temperature, it is vital to obtain functions that describe the trends to use them in FLUENT.

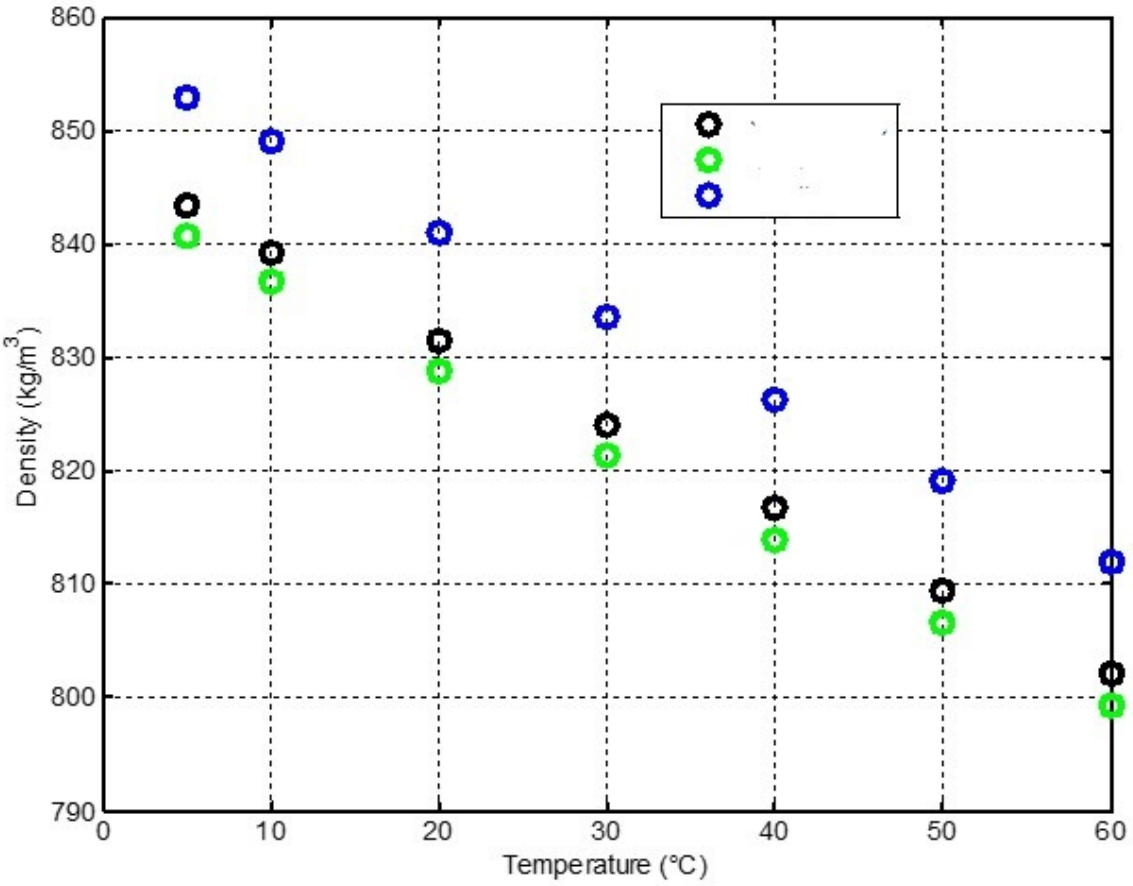

Figure D.1: Plot of crude oil density used to obtain coefficients for the Piecewise-polynomial function [15]

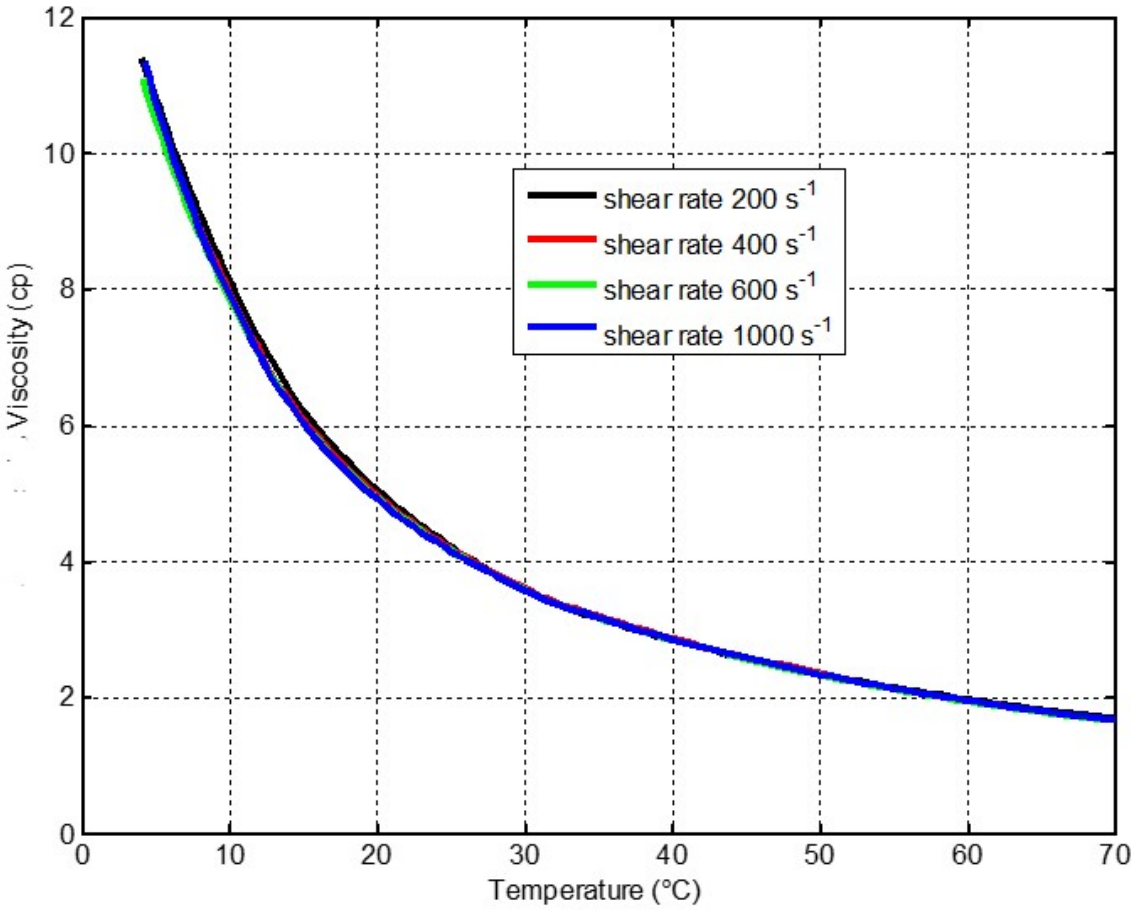

Figure D.2: Plot of crude oil viscosity used to obtain coefficients for the Piecewise-polynomial function [15]

E Temperature Profiles

Bulk fluid temperature contours for the flow simulations used in the sensitivity analysis are presented in this section. These temperature profiles illustrate bulk fluid temperature evolvement as a function of flow-time. It can be observed that the region with the highest temperature reduces more significantly with the 11.01 kg/s flow compared to the 33.03 kg/s. It indicates that cooling is slowest with higher rates due to continuous inflow of hot fluids into the tank at higher rates.

These contours can be used to locate potential areas vulnerable to wax appearance. From all the profiles, it can be seen that at steady state, wax is likely not to appear at the center of the bag since the fluid temperature at that region is higher than the WDT. Higher rates have minimal chances for wax to appear in most of the regions.

E.1 Simulations with 11.01 kg/s

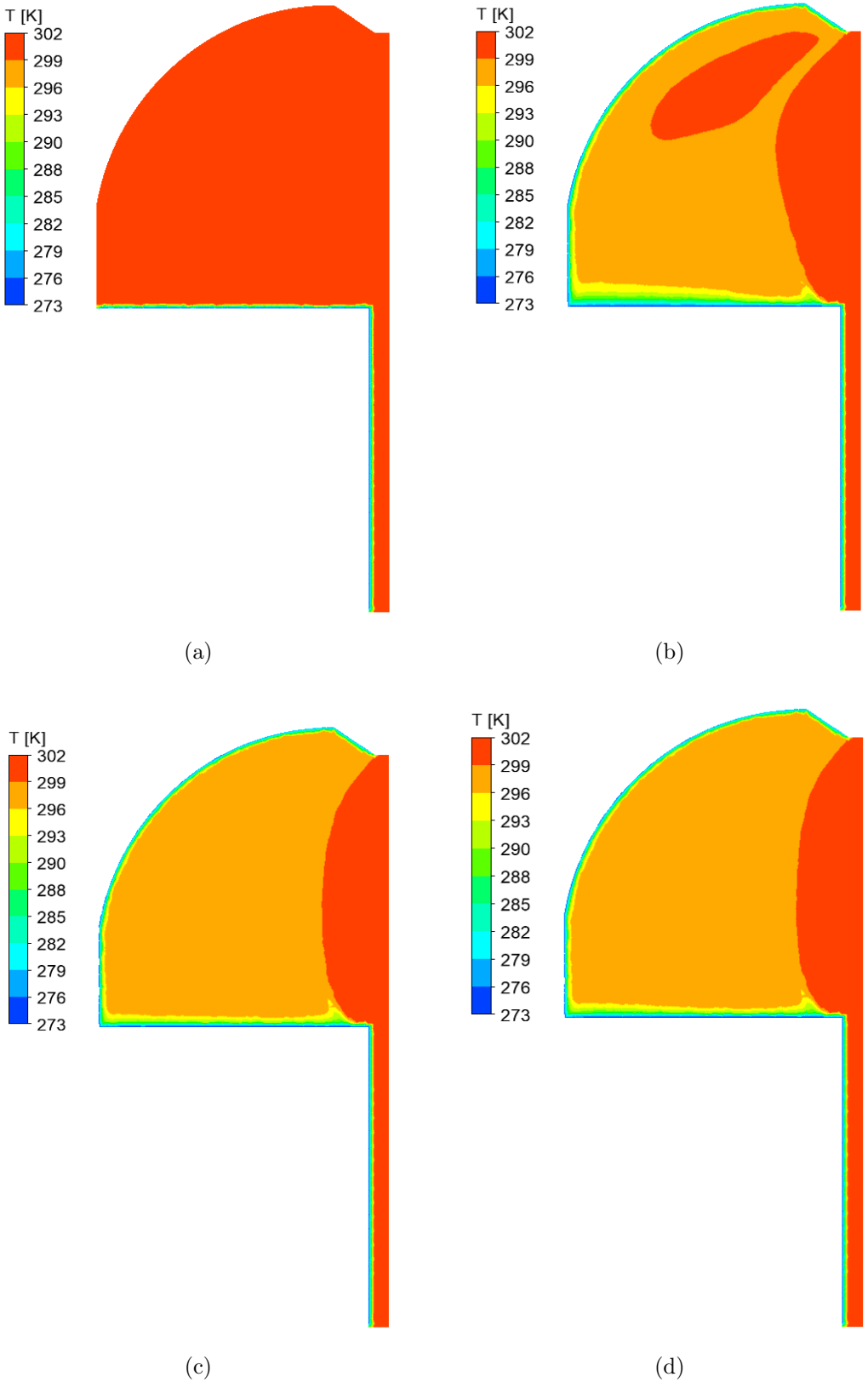

Figure E.1: Bulk fluid temperature evolution at different flow-times during 11.01 kg/s simulations (a) 100s (b) 471100s (c) 2271100s (d) steady state

E.2 Simulations with 22.02 kg/s

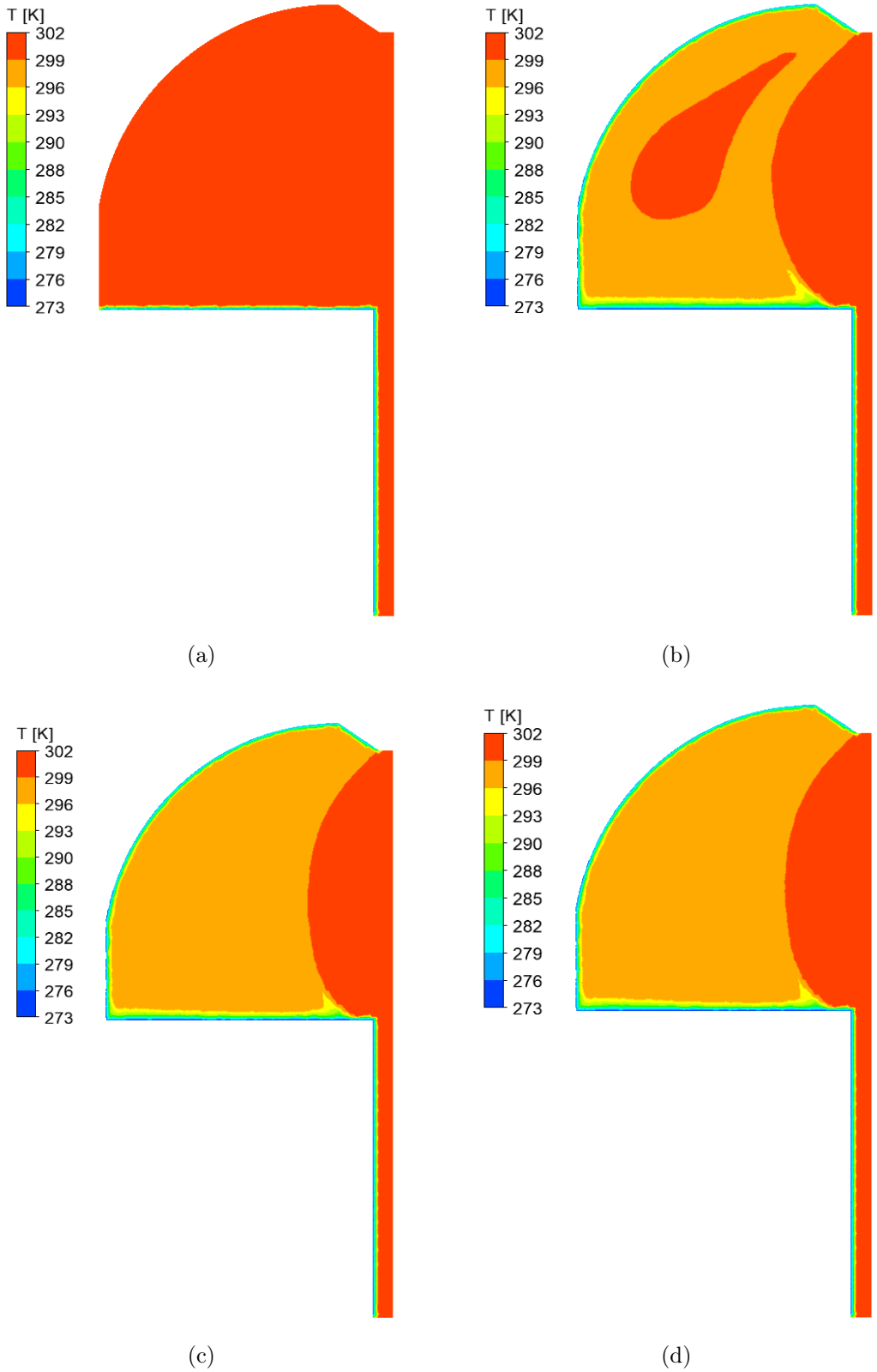

Figure E.2: Bulk fluid temperature evolution at different flow-times during 22.02 kg/s simulations (a) 100s (b) 471100s (c) 2271100s (d) steady state

E.3 Simulations with 33.03 kg/s

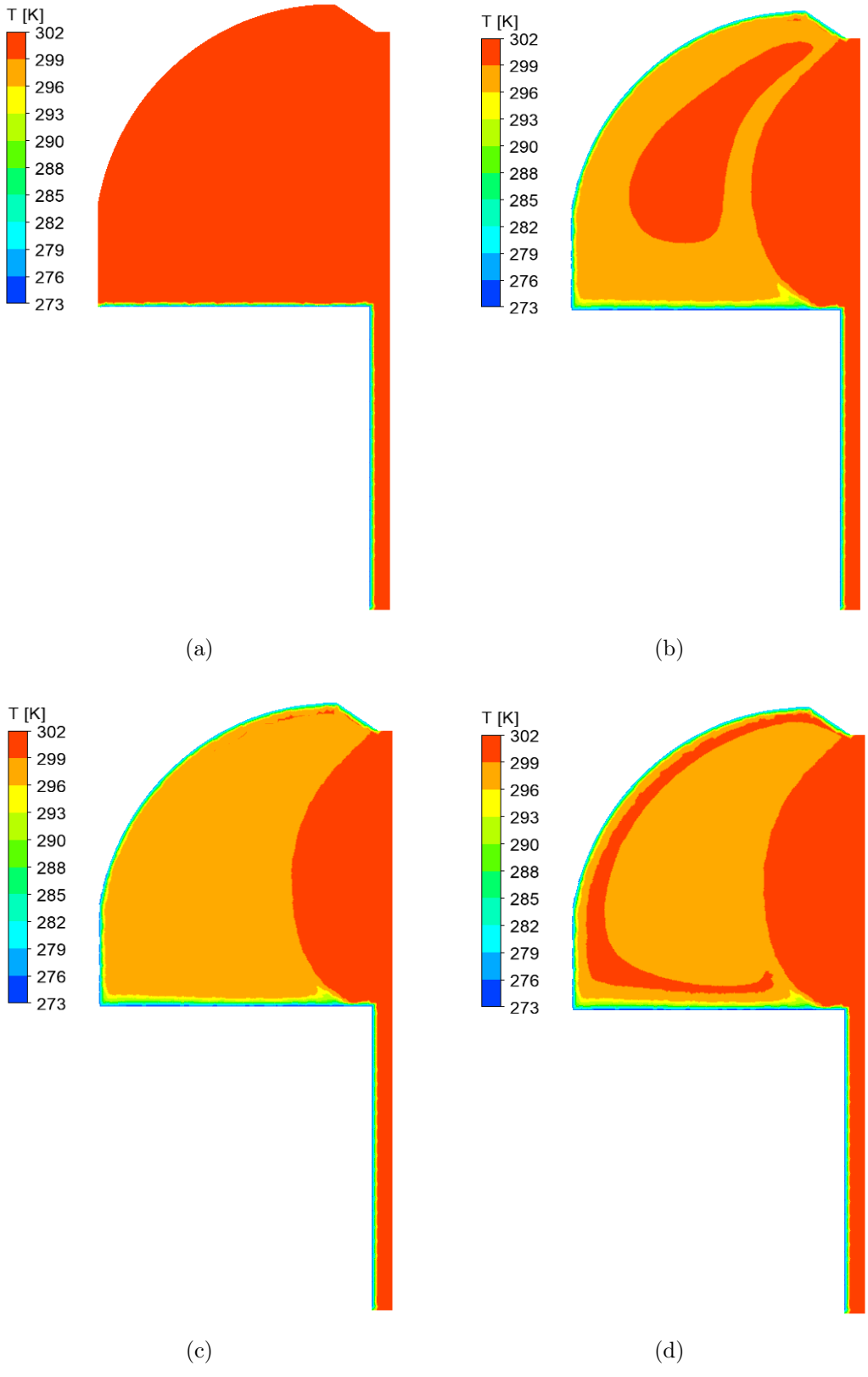

Figure E.3: Bulk fluid temperature evolution at different flow-times during 33.03 kg/s simulations (a) 100s (b) 471100s (c) 2271100s (d) steady state

F Velocity Profiles

Velocity contours for the no-flow and flow simulations used in this study are presented in this section. These velocity profiles illustrate magnitude of velocities and direction of the fluid molecules due to cooling as a function of flow-time. It can be observed that for no-flow simulations, molecules are seen to move downwards at the start of simulations then later followed by swirl movements. At the beginning of simulations there is cooling of the fluid starting from the walls. The cooled molecules become denser and start to move downwards to replace the warmer molecules.

The velocity profiles for the flow simulations indicate an upward movement of the molecules at the center of the bag and downwards at the sides. The region with the upward movement of the molecules increases with the increase in flowrate.

F.1 No-Flow Simulations

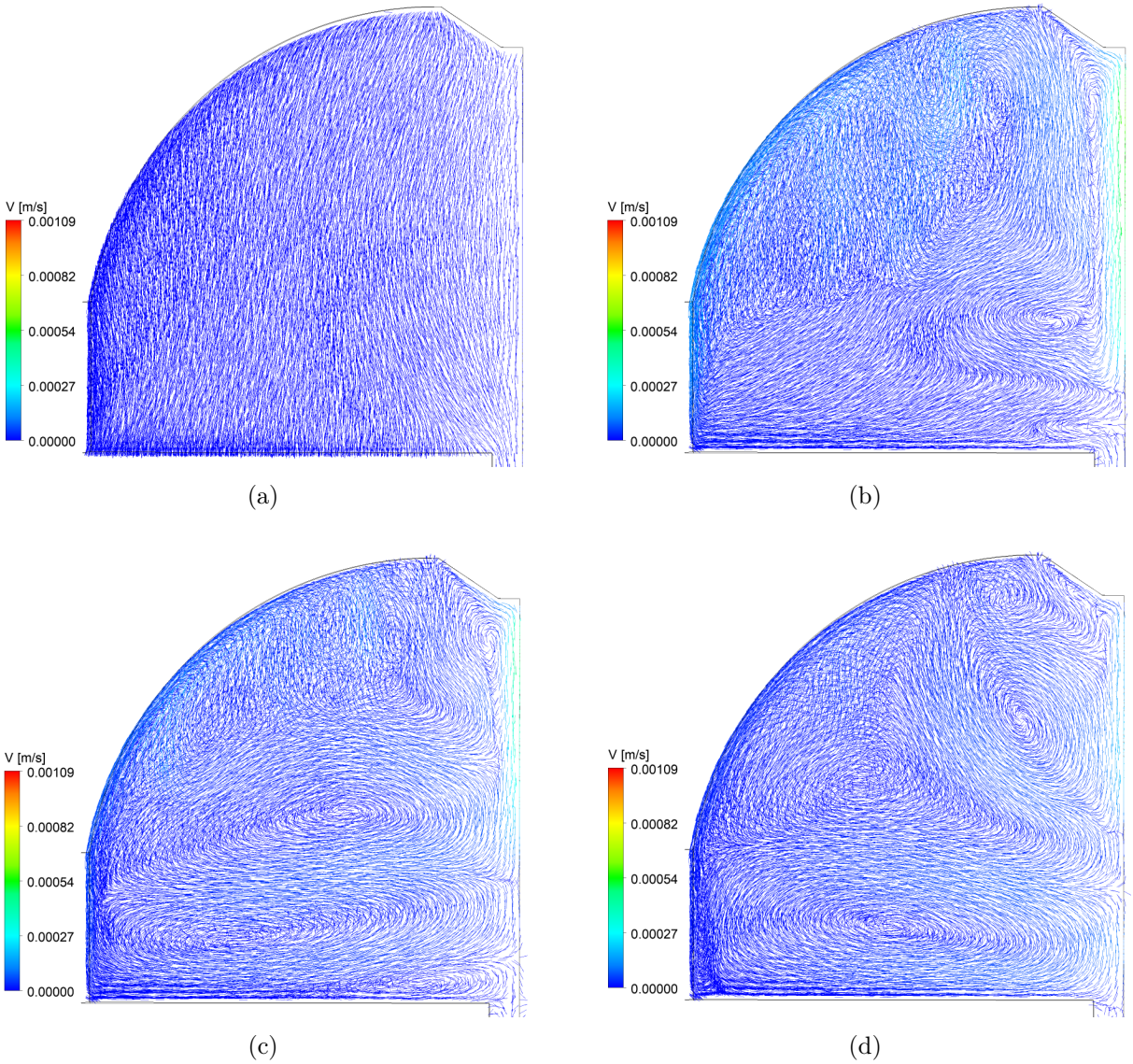

Figure F.1: Velocity vector during no-flow at (a) 100s (b) 471100s (c) 2271100s (d) steady state

F.2 Simulations with 11.01 kg/s

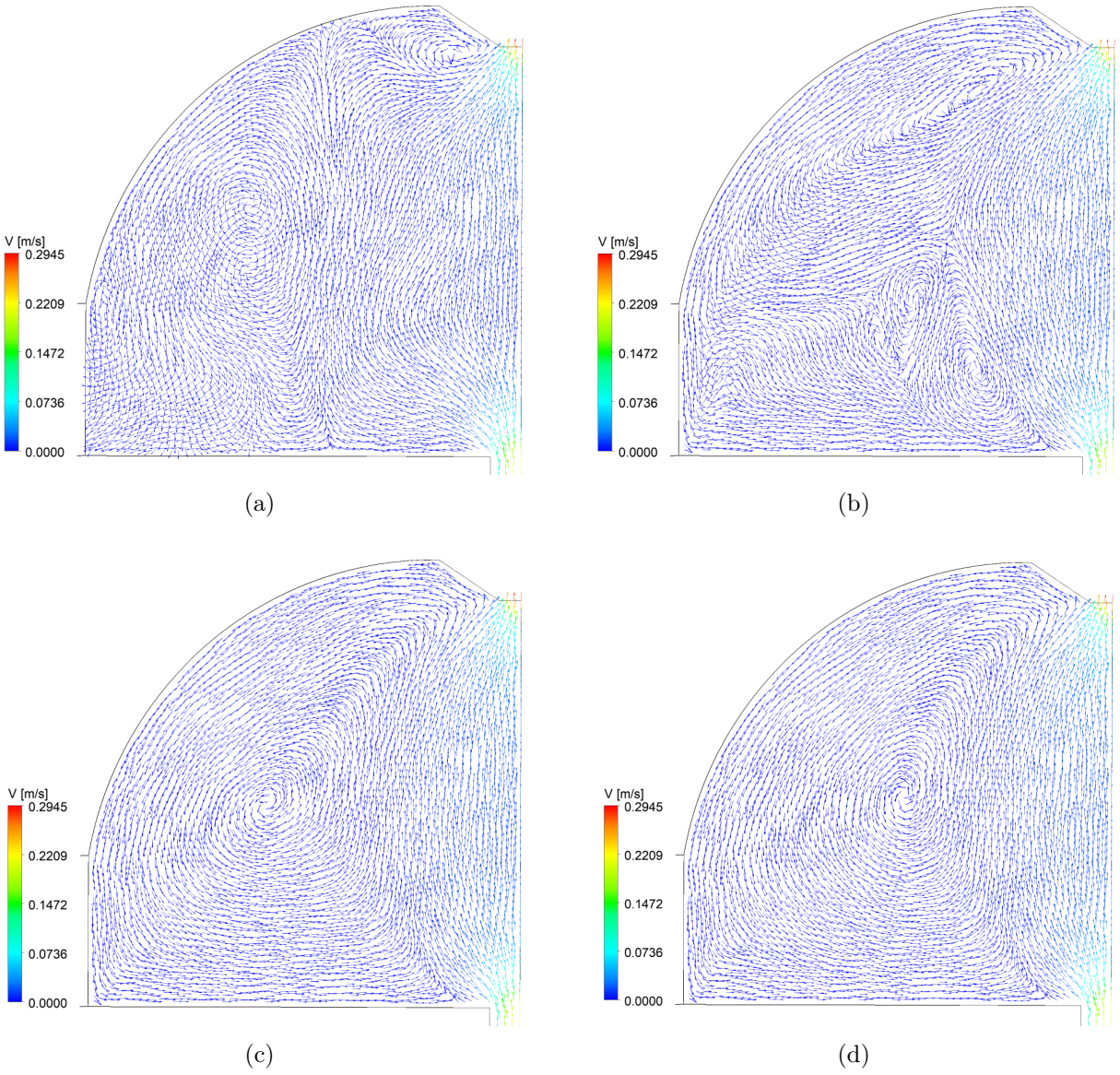

Figure F.2: Velocity vector during 11.01 kg/s flow at (a) 100s (b) 471100s (c) 2271100s (d) steady state

F.3 Simulations with 22.02 kg/s

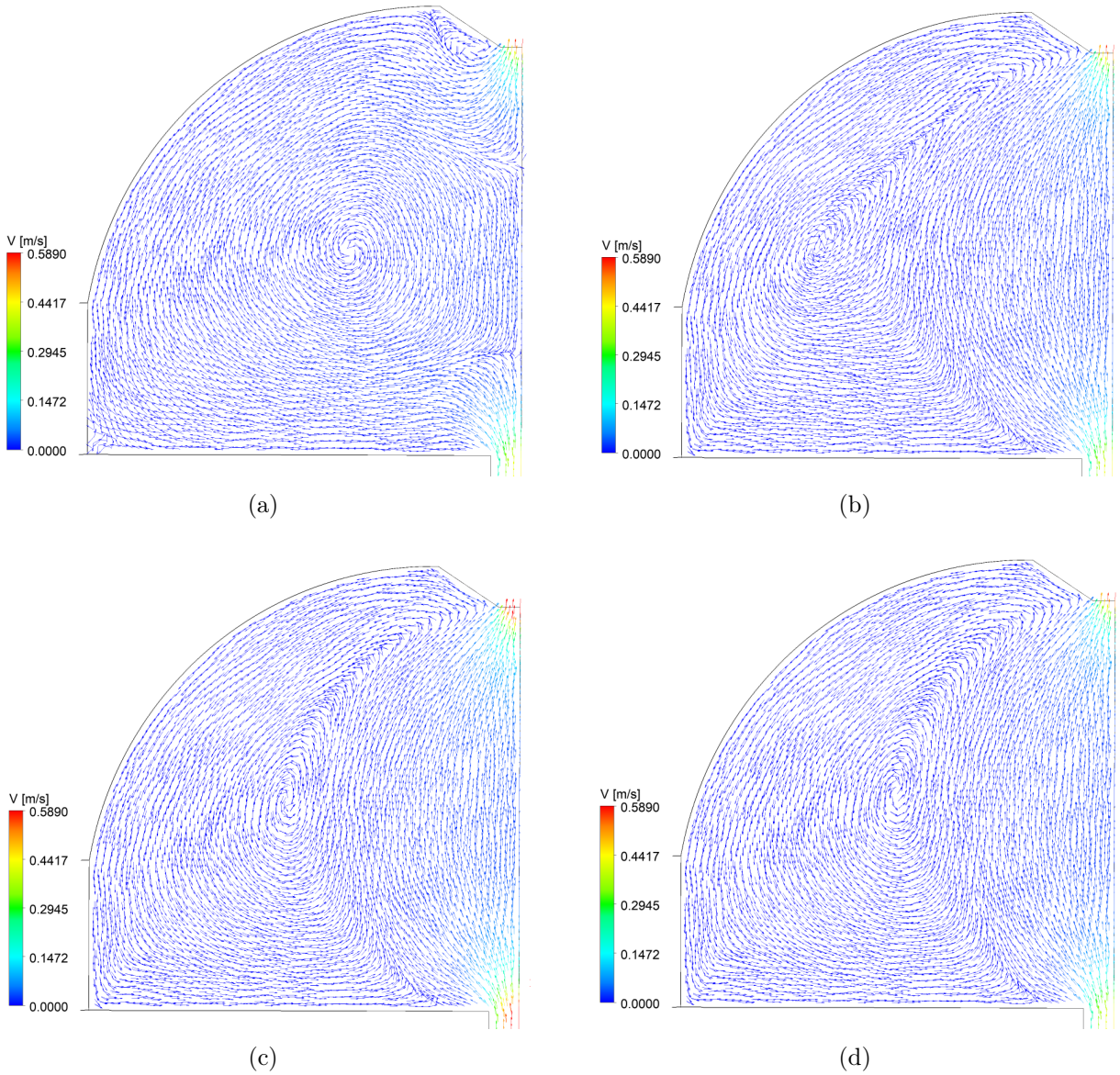

Figure F.3: Velocity vector during 22.02 kg/s flow at (a) 100s (b) 471100s (c) 2271100s (d) steady state

F.4 Simulations with 33.03 kg/s

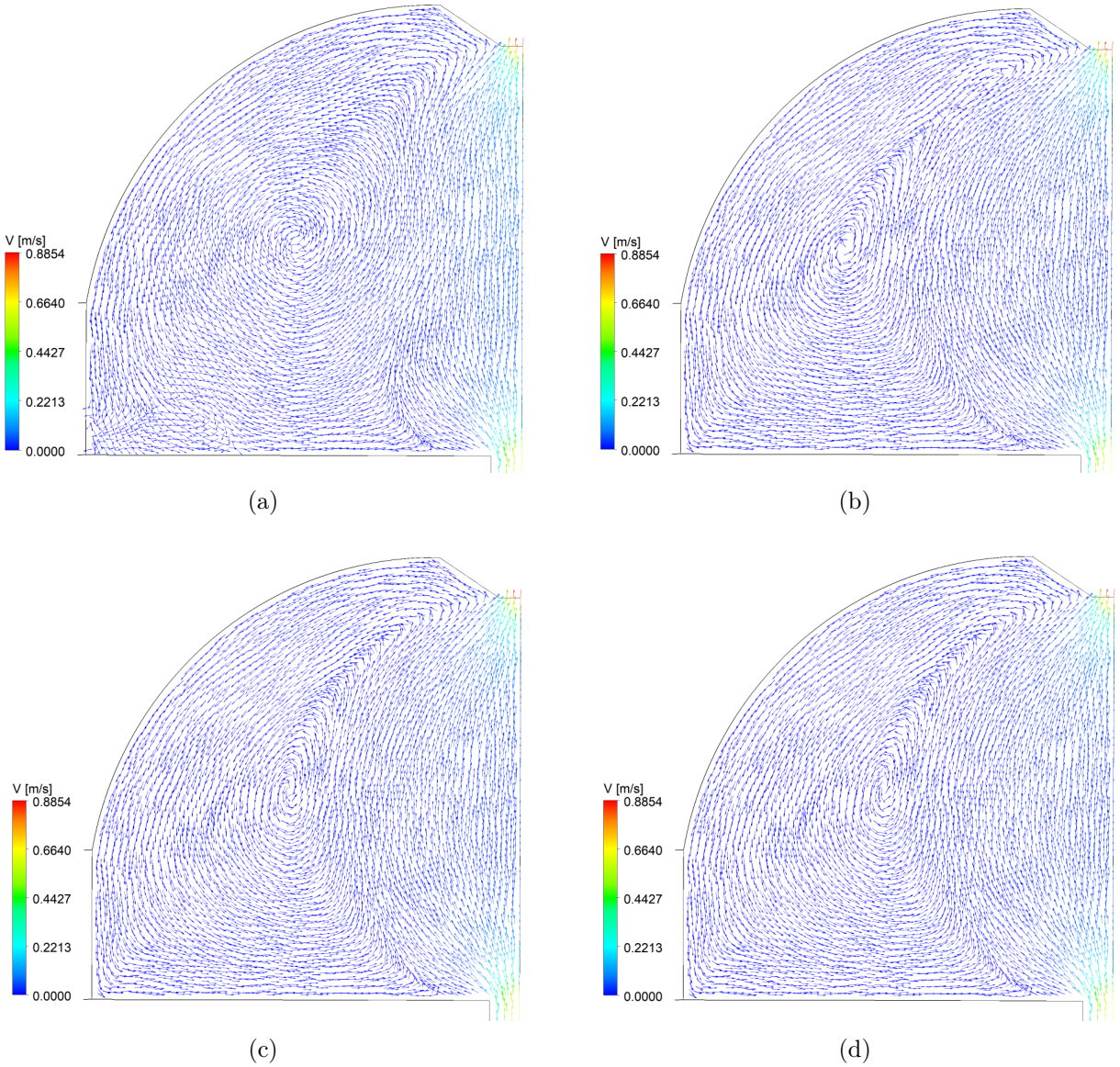

Figure F.4: Velocity vector during 33.03 kg/s flow at (a) 100s (b) 471100s (c) 2271100s (d) steady state

G Enlarged Figures of the Velocity Profiles for the Comparison Study between No-Flow and Flow Steady State Solutions

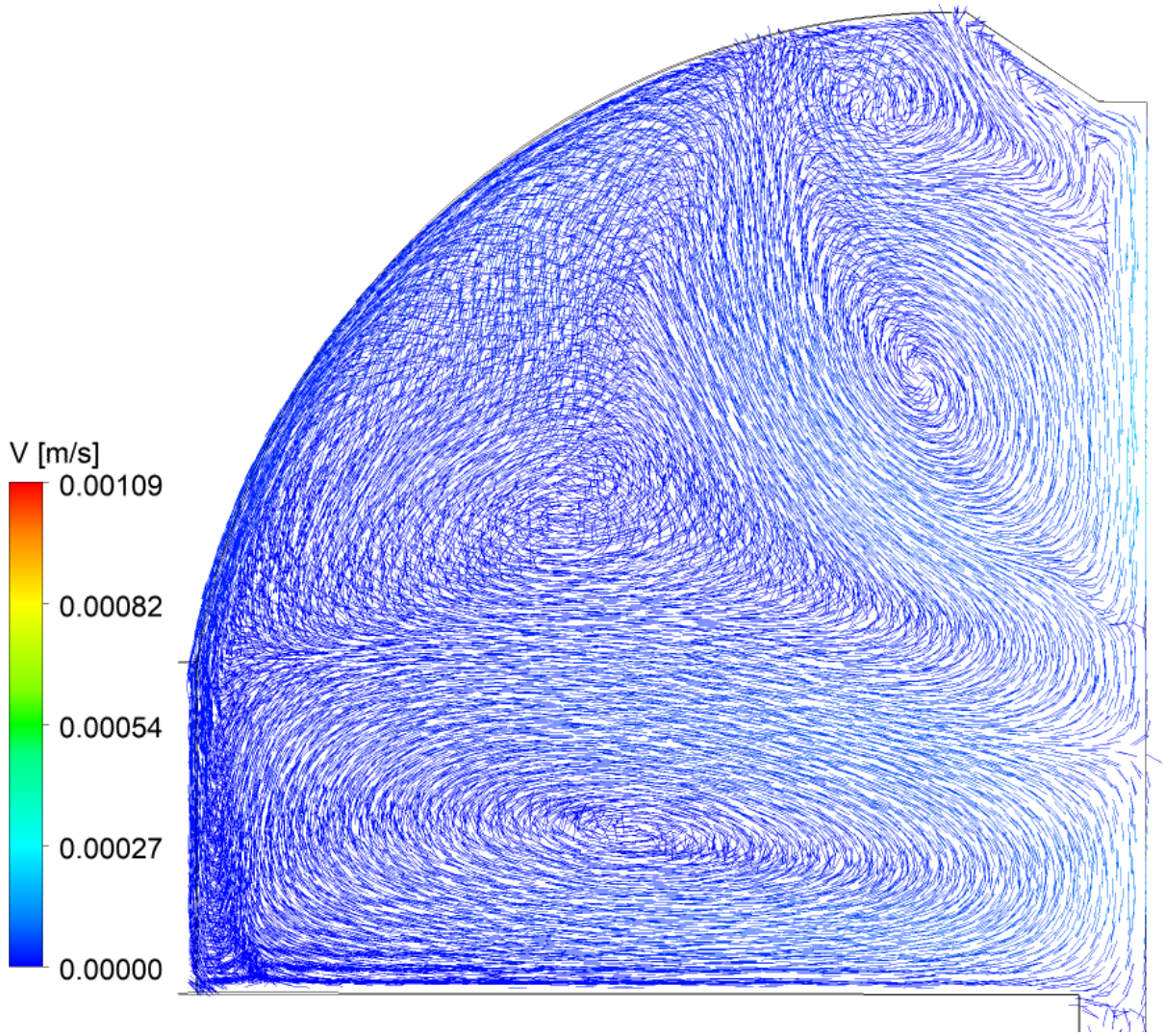

Figure G.1: Velocity vector from no-Flow Steady state Solution

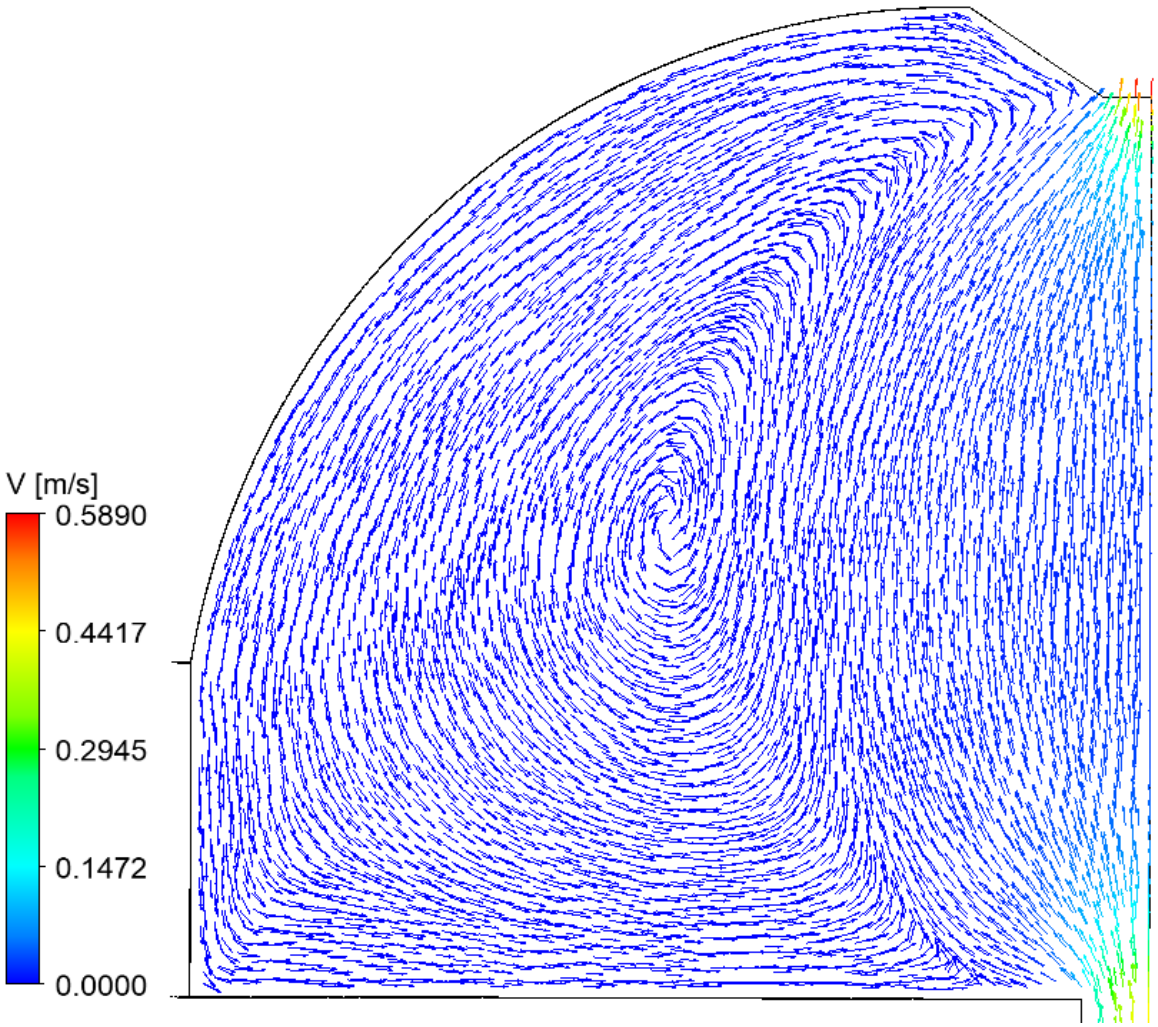

Figure G.2: Velocity vector from Flow Steady state Solution

H Steady State Solution of No-Flow Simulations

Locations that are vulnerable to wax appearance are determined when steady state solutions of no-flow and flow simulations are reached. For the no-flow simulations, a steady state solution is considered when there are minimal changes in fluid temperature at Point x as seen in Figure H.1

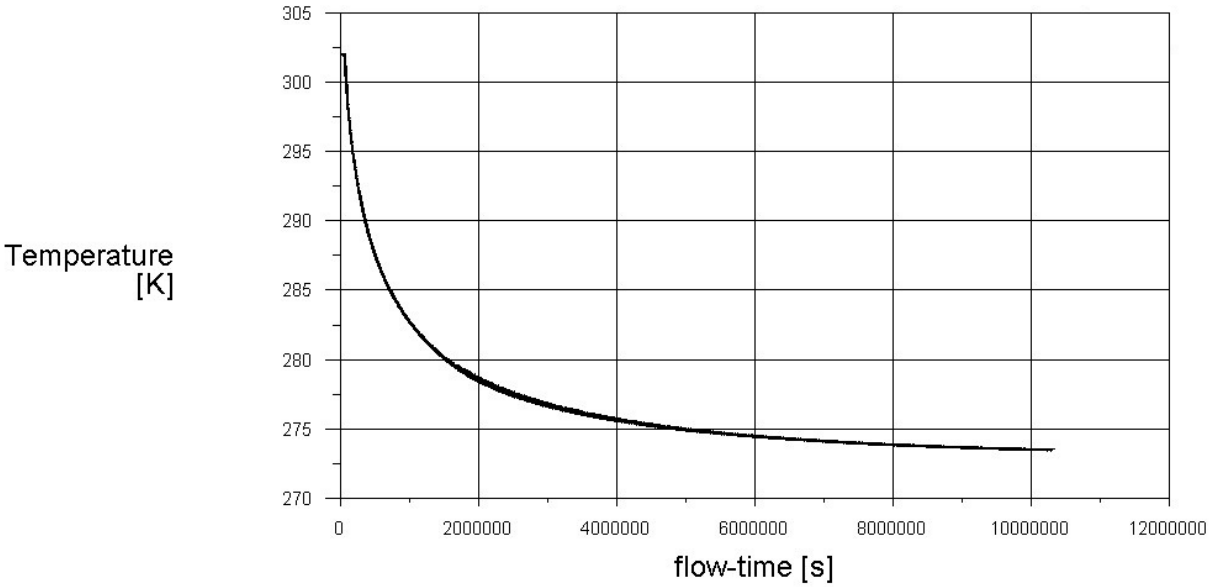

Figure H.1: Steady state solution of no-flow Simulations